Title

Investigation of Coupled THMC Processes and Reactive Transport: FY14 Progress

Authors

Rutqvist, Jonny
Davis, James
Zheng, Liange
et al.

Publication Date

2014-08-15

Investigation of Coupled THMC Processes and Reactive Transport: FY14 Progress

Fuel Cycle Research & Development

Prepared for

U.S. Department of Energy
Used Fuel Disposition Campaign

Jonny Rutqvist
James Davis
Liange Zheng
Victor Vilarrasa
James Houseworth
Jens Birkholzer

Lawrence Berkeley National Laboratory

August, 2014

FCRD-UFD-2014-000497

Revision 2
12/20/2012

APPENDIX E

FCT DOCUMENT COVER SHEET [1]

Name/Title of Deliverable/Milestone/Revision No.	Investigation of Coupled THMC Processes and Reactive Transport: FY14 Progress
Work Package Title and Number	Crystalline Disposal R&D - LBNL FT-14LB080704
Work Package WBS Number	1.02.08.07
Responsible Work Package Manager	James E. Houseworth (signature on file)
	(Name/Signature)

Date Submitted 08/15/2014

Quality Rigor Level for Deliverable/Milestone[2]	☐ QRL-3	☐ QRL-2	☐ QRL-1 ☐ Nuclear Data	☒ Lab/Participant QA Program (no additional FCT QA requirements)

This deliverable was prepared in accordance with Lawrence Berkeley National Laboratory
(Participant/National Laboratory Name)

QA program which meets the requirements of
☒ DOE Order 414.1 ☐ NQA-1-2000 ☐ Other

This Deliverable was subjected to:

☐ Technical Review ☐ Peer Review

Technical Review (TR)

Review Documentation Provided

☐ Signed TR Report or,
☐ Signed TR Concurrence Sheet or,
☐ Signature of TR Reviewer(s) below

Peer Review (PR)

Review Documentation Provided

☐ Signed PR Report or,
☐ Signed PR Concurrence Sheet or,
☐ Signature of PR Reviewer(s) below

Name and Signature of Reviewers

NOTE 1: *Appendix E should be filled out and submitted with the deliverable. Or, if the PICS:NE system permits, completely enter all applicable information in the PICS:NE Deliverable Form. The requirement is to ensure that all applicable information is entered either in the PICS:NE system or by using the FCT Document Cover Sheet.*

NOTE 2: *In some cases there may be a milestone where an item is being fabricated, maintenance is being performed on a facility, or a document is being issued through a formal document control process where it specifically calls out a formal review of the document. In these cases, documentation (e.g., inspection report, maintenance request, work planning package documentation or the documented review of the issued document through the document control process) of the completion of the activity along with the Document Cover Sheet is sufficient to demonstrate achieving the milestone. If QRL 1, 2, or 3 is not assigned, then the Lab/Participant QA Program (no additional FCT QA requirements box must be checked, and the work is understood to be performed, and any deliverable developed, in conformance with the respective National Laboratory/Participant, DOE- or NNSA-approved QA Program.*

This page is intentionally blank.

CONTENTS

FIGURES

TABLES

ACRONYMS

BBM	Barcelona Basic Model
BRGM	Bureau de Recherches Géologiques et Minières
CM	Chemical and Mechanical
DIS	Diffuse Ion Swarm
DSM	Dual-Structure Model
EBS	Engineered Barrier System
EDL	Electrical Double Layer
EDZ	Excavation Disturbed Zone
FEBEX	Full-scale Engineered Barriers Experiment
FEPs	Features, Events and Processes
LC	Loading-Collapse
MD	Molecular Dynamics
NBS	Natural Barrier System
NL	Neutral Line
OECD	Organisation for Economic Co-operation and Development
OSSC	Outer-Sphere Surface Complexes
PA	Performance Assessment
PB	Poisson-Boltzmann
PPPM	Particle-Particle Particle-Mesh
THMC	Thermal-Hydrological-Mechanical-Chemical
TLM	Triple-Layer Model
UDM	User-Defined Constitutive Model
UFD	Used Fuel Disposition

1. INTRODUCTION

The multi-barrier system in a nuclear waste repository typically consists of the natural barrier system (NBS), which includes the repository host rock and its surrounding subsurface environment, and the engineered barrier system (EBS). The EBS represents the man-made, engineered materials placed within a repository, including the waste form, waste canisters, buffer materials, backfill, and seals (OECD 2003).

Geological repositories in crystalline rock rely on clay buffers to provide hydrological and mechanical isolation of the waste and waste canisters from the host rock environment (Pusch et al. 2012, Lenhard et al. 2011). Smectite-rich clays (such as bentonite) have been identified as likely candidates for backfill/buffer inside access drifts and waste emplacement locations in crystalline-rock repositories (Pusch et al. 2012). In addition to their low permeability, strong sorption characteristics, and chemical buffering, smectite-rich clays are swelling clays that will fill up spaces left after initial emplacement, limiting water movement between the waste canister and the rock. Therefore, the clay buffer plays a significant role in the containment and long-term retardation of radionuclide release in crystalline rock.

During the lifespan of a geologic repository, the performance of the engineered barrier system (EBS), including the clay buffer, is affected by complex thermal, hydrogeological, mechanical, chemical, and biological processes, such as heat release due to radionuclide decay, multiphase flow (including gas release due to canister corrosion), swelling of buffer materials, radionuclide diffusive transport, waste dissolution, and chemical reactions. An in-depth understanding of these coupled processes is critical for the performance assessment (PA) of an EBS and the entire repository. Within the crystalline rock work package of the Used Fuel Disposition (UFD) Campaign, LBNL's research is currently focused on two relevant areas related to clay buffer materials (bentonite), namely (1) thermal-hydrological-mechanical-chemical (THMC) processes, and (2) diffusive transport. The long-term goal of this work is to develop and verify models that can simulate these processes. The models can then be used to help provide a full understanding of how coupled processes impact interactions between the EBS components and the near-field host rock and radionuclide release and transport in the EBS.

LBNL's focus areas address key Features, Events and Processes (FEPs), which have been ranked in importance from medium to high, as listed in Tables 7 and 8 of the *Used Fuel Disposition Campaign Disposal Research and Development Roadmap* (FCR&D-USED-2011-000065 REV0) (Nutt 2011). Specifically, they address FEP 2.2.01, Excavation Disturbed Zone (EDZ) for shale by investigating the effects of coupled processes on interactions between shale (clay) disposal formations and the EBS; FEP 2.1.04.01, Buffer/Backfill; FEPs 2.1.07.02, 03, 04, 09, Mechanical Processes; FEPs 2.1.08.03, 07, 08, Hydrologic Processes; and FEP 2.1.11.04, Thermal Processes, by studying coupled processes in the EBS; and FEPs 2.1.09.52, 53, 54, Chemical Processes—Transport, by investigating reactive-diffusive radionuclide transport in bentonite.

This report documents the progress that LBNL has made in its two R&D focus areas in FY14. Chapter 2 presents the modeling results of THMC processes within bentonite and the interaction between the EBS and a clay disposal formation in the near field. Chapter 3 documents the development of reactive-diffusive transport modeling approaches for radionuclide migration in bentonite. A summary and discussion of future work activities are given in Chapter 4.

2. MODELING COUPLED THMC PROCESSES IN THE EBS

The long-term chemical and mechanical stability of protective bentonite buffers and tunnel backfill is a key issue in the long-term performance of backfilled, multiple barrier nuclear waste repositories. For example, a certain swelling pressure should be maintained to keep the buffer homogenous, to prevent canister sinking, to prevent the adverse effect of external rock shear movements, to limit colloid transport, and to prevent the buffer from being a preferred pathway of radionuclide transport. The long-term stability of the buffer is governed by coupled thermal-hydrological-mechanical and chemical (THMC)

processes. These coupled THMC processes can be simulated by numerical modeling, e.g., by a coupling of LBNL's TOUGHREACT reactive transport simulator to a geomechanical code such as FLAC3D. However, this requires appropriate constitutive models describing couplings between the different processes.

In this section, we describe our ongoing work toward developing and applying coupled THMC models for the analysis of EBS coupled processes. We have previously implemented the Barcelona Basic Model (BBM) into the TOUGH-FLAC simulator for modeling coupled THM processes in bentonite, and have also developed a simplified approach that linked this model to chemical processes by coupling to the reactive transport simulator TOUGHREACT. This development and the results were summarized in a peer-reviewed journal article entitled "Modeling of Coupled Thermo-Hydro-Mechanical Processes with Links to Geochemistry Associated with Bentonite-Backfilled Repository Tunnels in Clay Formations," which has recently been published in *Rock Mechanics and Rock Engineering* (Rutqvist et al. 2014). The mechanical-chemical coupling approach in that study was focused on the evolution of primary and secondary swelling, in which the secondary swelling was caused by changes in ionic concentration. The model was used to simulate the effects of salt concentration on the swelling stress.

In the FY2013 milestone report "Investigation of Reactive Transport and Coupled THMC Processes in the EBS" (Davis et al., 2013), we presented progress toward the implementation and testing of a dual-structure model for expansive clay into TOUGH-FLAC. In a dual-structure model, the material consists of two structural levels: a microstructure in which the interactions occur at the particle level, and a macrostructure that accounts for the overall fabric arrangement of the material comprising aggregates and macropores (Figure 2.1) (Gens et al. 2006, Sánchez et al. 2005, Gens and Alonso 1992). A dual-structure model has important features for modeling the mechanical behavior of a bentonite buffer, such as irreversible strain during suction cycles. However, most importantly, a dual-structure model provides the necessary link between chemistry and mechanics, enabling us to develop a fully coupled THMC model for the analysis of long-term EBS behavior. This approach enables mechanistic modeling of processes important for long-term buffer stability, including the effects of pore-water salinity on swelling (loss of swelling), conversion of smectite to nonexpansive mineral forms (loss of swelling), and swelling pressure versus exchangeable cations. In the FY2013 milestone report (Davis et al. 2013), we presented and applied one approach suggested by Gens (2010) for linking chemistry to the bentonite mechanics through the dual-structure model. In Gens' (2010) approach, some of the parameters related to micro-structural swelling depend on the concentration of each exchangeable cation.

In FY2014, we have made further significant progress in the development, testing, and application of the dual-structure model, as presented in this section of the milestone report. This includes additional testing and a demonstration of the capability of the implemented dual-structure model by modeling and reproducing observed behavior in a laboratory test of expansive clay. As observed in the experiments, the simulations yield nonreversible strain accumulation upon suction cycles and a decreasing swelling capacity with increasing confining stress. Finally, we present model simulations of a generic high-level nuclear waste repository with waste emplacement in horizontal tunnels backfilled with expansive clay and hosted in a clay rock formation. To our knowledge, this is the first time a dual-structure model has been applied to model coupled THM processes of a repository over a 100,000-year time period. We compared the THM results of the dual-structure model with those of the standard single-structure BBM, showing the importance of considering the dual-structure behavior of the expansive bentonite buffer material. We also upgrade the chemical and mechanical (CM) coupling scheme. Now the microstructural swelling depends not only the concentration of exchangeable cations, as implemented in FY2013 report (Davis et al. 2013), but also the mass fraction of smectite and the ion concentration of pore water. This coupling scheme needs to be validated with experimental data, and its effect on the long-term THMC behavior of EBS bentonite will be evaluated through THMC models that adopt dual-structure model and the upgraded CM coupling scheme in the future.

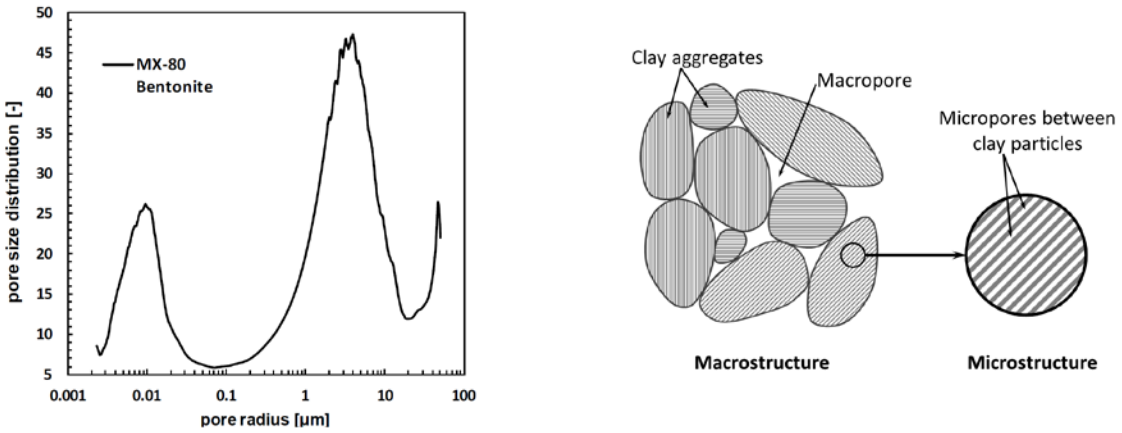

Figure 2.1. (a) Pore size distribution and (b) schematic representation of the two structural levels considered in the dual-structure model. Clay particles are represented by the gray lines.

2.1 Dual-Structure Model Implementation in TOUGH-FLAC

In this section, we present the development and implementation of a dual-structure model for expansive soils into TOUGH-FLAC. We first present an overview of the basic equations in the dual-structure model. We then summarize the implementation of this model into TOUGH-FLAC.

2.1.1 The Dual-Structure Approach

The dual-structure model considers the existence of a macrostructure, a microstructure, and the interactions between them. The macrostructure can be modeled with a constitutive model for unsaturated soils, such as the BBM. The BBM is able to describe many typical features of the mechanical behavior of unsaturated soils, including wetting-induced swelling or collapse strains (depending on the magnitude of the applied stress), as well as the increase in shear strength and apparent pre-consolidation stress with suction (Gens et al. 2006). The extension of BBM to a dual-structure model enables simulating the behavior of expansive soils, such as the dependency of swelling strains and swelling pressures on the initial stress state and on the stress path, strain accumulation upon suction cycles and secondary swelling. It is believed that such behavioral features are mainly related to the existence of coupled chemical-hydrogeological-mechanical phenomena between distinct levels of structure within the material (Alonso et al. 1999).

Conceptually, in a dual-structure model, as described by Alonso et al. (1999) and Sánchez et al. (2005), the total volume, V, of the material consists of the solid phase, V_s, the microstructural voids V_{vm}, and the macrostructure voids V_{vM}

$$V = V_s + V_{vm} + V_{vM} = V_m + V_{vM} \quad , \tag{2.1}$$

where V_m is the volume of the microstructure.

Additionally, the total void ratio, e, and porosity, ϕ, are the sum of their microstructural and macrostructural components according to

$$e = \frac{V_v}{V_s} = \frac{V_{vM}}{V_s} + \frac{V_{vm}}{V_s} = e_M + e_m, \tag{2.2}$$

$$\phi = \frac{V_v}{V} = \frac{V_{vM}}{V} + \frac{V_{vm}}{V} = \phi_M + \phi_m, \tag{2.3}$$

where V_v is the total volume of voids and the subscripts m and M refer to the microstructure and the macrostructure, respectively.

The microstructure can swell to invade the macroporosity, depending on the mechanical confinement and load level. This is relevant when considering permeability changes during the expansive soil swelling, because fluid flow takes place through the macroporosity, which is not proportional to the total strain and deformation of the expansive soil.

2.1.2 Macrostructural Level

The macrostructural behavior is modeled based on the BBM, in which the yield surface is defined in the $p-q-s$ space, where p is net mean stress (i.e., total stress minus gas-phase pressure), q is deviatoric stress (or shear stress), and s is suction (i.e., gas pressure minus liquid pressure). The size of the elastic domain increases as suction increases. This is shown in Figure 2.2 in the isotropic stress (*s*-*p* space) plane. The rate of increase of the elastic domain, represented by the loading-collapse (LC) curve, is one of the fundamental characteristics of the BBM (Gens et al. 2006).

The suction-dependent loading-collapse (LC) yield surface bounds the elastic region according to

$$f_{LC} = \frac{q^2}{g_y(\theta)^2} - \frac{M^2}{g_y(\theta=0)^2}(p+p_s)(p_0-p) = 0 \tag{2.4}$$

where θ is the Lode angle, the function $g_y(\theta)$ describes the shape of the yield surface in the deviatoric plane, M is the constant slope of the critical state line, $p_s = k_s s$ represents the increase in cohesion with suction, k_s is an empirical material constant and the function

$$p_0 = p^c \left(\frac{p_0^*}{p^c} \right)^{[\lambda_{Ps0} - \kappa_{Ps0}]/[\lambda_{Ps} - \kappa_{Ps0}]} \tag{2.5}$$

is the net mean yield stress (or apparent pre-consolidation stress) at the current suction, where p_0^* is the net mean yield stress (or pre-consolidation stress) at full saturation, p^c is a reference stress, λ_{Ps0} is a compressibility parameter in virgin soil states at zero suction, $\lambda_{Ps} = \lambda_{Ps0}\left[(1-r)\exp(-\xi s) + r\right]$ is a compressibility parameter in virgin soil states at suction *s*, and *r* is a constant related to the maximum stiffness of the soil (for an infinite suction), ξ is a parameter that controls the rate of increase of soil stiffness with suction, and κ_{Ps0} is the elastic stiffness parameter for changes in net mean stress at zero suction.

The flow rule is given by

$$g_{LC} = \frac{\alpha_a q^2}{g_y(\theta)^2} - \frac{M^2}{g_y(\theta = 0)^2}(p + p_s)(p_0 - p) \tag{2.6}$$

where α_a is a parameter that gives rise to a non-associative model, i.e., $g_{LC} \neq f_{LC}$.

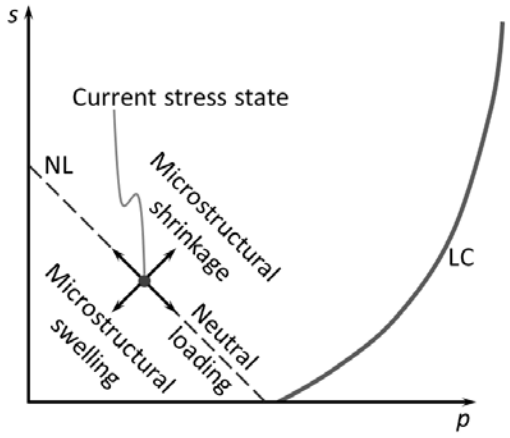

Figure 2.2. Schematic representation of the dual-structure model in the isotropic plane, including the neutral line (NL) and the loading-collapse (LC) yield surface. The NL moves with the current stress state, so that the current stress state is always contained within the NL. The stress state can change following one three stress paths: (i) microstructural shrinkage, if it moves to the right of the NL, (ii) microstructural swelling, if it moves to the left of the NL and (iii) neutral loading, if it moves along the NL, in which case the microstructure does not deform.

2.1.3 Microstructural Level

The following assumptions are adopted related to microstructural behavior and its interaction with the macrostructure:

- The microstructure is mainly saturated and the effective stress concept holds.
- The microstructural behavior is elastic and volumetric.
- Mechanical, hydraulic, and chemical equilibrium exists between microstructure and macrostructure.
- Coupling between microstructure and macrostructure results in a possible buildup of macrostructural elastoplastic strains when elastic microstructural strains occur.

With these assumptions, the volumetric microstructural strain, $\mathrm{d}\varepsilon_{vm}^{e}$, depends exclusively on variations in mean effective stress, $\mathrm{d}\hat{p} = \mathrm{d}(\bar{p} - p_l) = \mathrm{d}(\bar{p} - p_g + p_g - p_l) = \mathrm{d}(p + s)$, where $\bar{p}$ is mean stress, p_l is liquid phase pressure and p_g is gas phase pressure. Therefore, a straight line $p + s = constant$ can be drawn in the *p*-*s* space around the current state of stress and suction along which no microstructural strain takes place (Figure 2.2). This line, called the neutral line (NL), moves with the current stress state (C) and separates at each instant the zone of microstructural swelling from the zone of microstructural shrinkage in the $p - s$ plane (Figure 2.2).

2.1.4 Interaction Between Structural Levels

Microstructural swelling/shrinkage affects the structural arrangement of the macrostructure, inducing irreversible strains in the macroporosity. These irreversible macrostructural deformations induced by microstructural effects are considered proportional to the microstructural strain through interaction functions as

$$\mathrm{d}\varepsilon_{v\beta}^{p} = f\mathrm{d}\varepsilon_{vm}^{e} \tag{2.7}$$

where $\varepsilon_{v\beta}^{p}$ is the macrostructural plastic strain arising from the interaction between both structures. Two interaction functions are defined: $f = f_c$ for microstructural compression or shrinkage paths and $f = f_s$ for microstructural swelling paths. These functions can adopt several forms (Sánchez et al., 2005), but they always depend on the ratio p/p_0

$$f_c = f_{c0} + f_{c1}\left(p/p_0\right)^{n_c} \text{ and } f_s = f_{s0} + f_{s1}\left(1-p/p_0\right)^{n_s}, \tag{2.8a}$$

or

$$f_c = f_{c0} + f_{c1}\tanh\left[f_{c2}\left(p/p_0 - f_{c3}\right)\right] \text{ and } f_s = f_{s0} - f_{s1}\tanh\left[f_{s2}\left(p/p_0 - f_{s3}\right)\right], \tag{2.8b}$$

where f_{ij} and n_i ($i = \{c,s\}$ and $j = \{0,1,2,3\}$) are constants.

The ratio p/p_0 is a measure of the distance from the current stress state to the yield locus for the macrostructure LC, and its inverse has the same meaning as the overconsolidation ratio for an isotropically consolidated soil. A low p/p_0 implies a dense packing of the material. Under such dense packing (dense macrostructure), the microstructural swelling strongly affects the global arrangement of clay aggregates, which becomes more open. This results in a softening of the macrostructure, which implies that the macrostructural yield surface LC shrinks. Under this condition, expansion accumulates upon suction cycles. On the other hand, a high p/p_0 implies a looser macrostructure. Under such loose packing conditions, the microstructural swelling produces an invasion of the macropores, which tends to close the macrostructure, and compression accumulates upon suction cycles. In such a case, the elastic domain increases and LC expands (Alonso et al. 1999; Sánchez et al. 2005).

2.1.5 Elastic Strain

Equivalently to the BBM model, the macrostructural volumetric elastic strain increment for the dual-structure model is associated with changes in net mean stress $\mathrm{d}p$ and suction $\mathrm{d}s$ (Alonso et al. 1999)

$$\mathrm{d}\varepsilon_{vM}^{e} = \frac{1}{K_M}\mathrm{d}p + \frac{1}{K_s}\mathrm{d}s, \tag{2.9}$$

where K_M is the macrostructural bulk modulus and K_s is the macrostructural modulus associated with suction strain. K_M and K_s are defined as

$$K_M = \frac{\left(1+e_M\right)p}{\kappa_{Ps}\left(s\right)}, \tag{2.10}$$

$$K_s = \frac{(1+e_M)(s+p_{atm})}{\kappa_{sp}(p,s)} \tag{2.11}$$

where $\kappa_{Ps} = \kappa_{Ps0}(1+s\alpha_{ps})$, $\kappa_{sp} = \kappa_{sp0}(1+\alpha_{sp}\ln(p/p_{ref}))\exp(\alpha_{ss}s)$, κ_{Ps0}, κ_{sp0} are compressibility parameters for changes in net mean stress and suction, respectively, p_{ref} is a reference stress state for relating elastic compressibility to suction, and α_{ps}, α_{sp} and α_{ss} are empirical parameters.

The microstructural volumetric strain depends on the change in the microstructural effective stress

$$\mathrm{d}\varepsilon_{vm}^{e} = \frac{1}{K_m}\mathrm{d}\hat{p}, \tag{2.12}$$

where K_m is the microstructural bulk modulus for changes in mean effective stress $d\hat{p}$ Alonso et al. (1999) define two alternative expressions for the microstructural modulus

$$K_m = \frac{(1+e_m)\hat{p}}{\kappa_m}, \tag{2.13a}$$

$$K_m = \frac{e^{\alpha_m \hat{p}}}{\beta_m}, \tag{2.13b}$$

where κ_m, α_m and β_m are compressibility parameters.

Thermal strains are purely volumetric

$$\mathrm{d}\varepsilon_{v}^{T} = (\alpha_0 + 2\alpha_2\Delta T)\mathrm{d}T, \tag{2.14}$$

where α_0 and α_2 are material parameters corresponding to a temperature-dependent volumetric thermal expansion coefficient, T is temperature, and $\Delta T = T - T_0$, where T_0 is a reference temperature. Finally, dT is the change in temperature from the initial temperature, which could be different from T_0.

The deviatoric elastic strain increment is defined as

$$\mathrm{d}\varepsilon_{q}^{e} = \frac{1}{3G}\mathrm{d}q, \tag{2.15}$$

where G is the shear modulus and may be obtained using a constant Poisson ratio ν in

$$G = \frac{3(1-2\nu)}{2(1+\nu)}K_M. \tag{2.16}$$

Thus, the equations for elastic mechanical strain indicate the dependency of bulk modulus on suction (and hence fluid saturation), which in a dry clay can be significantly stiffer than in a water-saturated clay.

In total, the BBM is characterized by 18 parameters, with the dual-structure model incorporating between 8 and 11 additional parameters, depending on the microstructural bulk modulus and the interaction functions that are used.

2.1.6 Plastic Strain

Macrostructural plastic strain occurs by two possible mechanisms: either when the stress lies on the LC yield surface, or as a result of microstructural shrinkage/swelling. While the plastic strain by microstructural shrinkage/swelling is described by Eq. (2.7), the LC plastic strains are obtained from the plastic flow rule:

$$\mathrm{d}\varepsilon_{vLC}^{p} = \mathrm{d}\Lambda \frac{\partial g_{LC}}{\partial p}, \tag{2.17}$$

$$\mathrm{d}\varepsilon_{qLC}^{p} = \mathrm{d}\Lambda \frac{\partial g_{LC}}{\partial q}, \tag{2.18}$$

where $\mathrm{d}\Lambda$ is the plastic multiplier obtained from the consistency condition $\mathrm{d}f_{LC} = 0$ (recall Equation (2.4)). The calculation of the plastic multiplier $\mathrm{d}\Lambda$ is detailed in Rutqvist et al. (2011).

The total plastic volumetric strain is the sum of both plastic mechanisms:

$$\mathrm{d}\varepsilon_{v}^{p} = \mathrm{d}\varepsilon_{vLC}^{p} + \mathrm{d}\varepsilon_{v\beta}^{p}. \tag{2.19}$$

The hardening variable of the macrostructure — the pre-consolidation pressure p_0^* —depends on the total plastic volumetric strain ε_v^p as

$$\frac{\mathrm{d}p_0^*}{p_0^*} = \frac{(1+e_M)\mathrm{d}\varepsilon_v^p}{\lambda_{Ps0} - \kappa_{Ps0}}. \tag{2.20}$$

2.1.7 Implementation into TOUGH-FLAC

We implemented the dual-structure model in TOUGH-FLAC, by extending our previous implementation of the BBM (Rutqvist et al. 2011) to include the microstructural level and its interactions with the macrostructure. This involves consideration of the sequential coupling of the TOUGH2 and FLAC^{3D} simulators (Rutqvist et al. 2011), and constitutive stress-strain behavior in FLAC^{3D}. TOUGH2 is a multiphase nonisothermal finite volume code; FLAC^{3D} is a geomechanics finite difference code. Our implementation of the dual-structure model in FLAC^{3D} was done using the user-defined constitutive model (UDM) option in FLAC^{3D}, including C++ coding and dynamic link libraries. Specifically, the following calculation items were added:

1. Microstructural strain and effective stress
2. Macrostructural strain
3. Global elastic tensor depending on microscopic and macroscopic structural compliances
4. Micro/macrostructural interaction functions
5. Plastic macrostructural strain from structural interactions
6. Plastic corrections in the FLAC^{3D} elastoplastic algorithm
7. Plastic hardening/softening factors.

Finally, at the end of each FLAC^{3D} step, the hardening parameter, i.e., the pre-consolidation pressure p_0^*, the bulk modulus of both microstructure and macrostructure and the tangential bulk modulus, are updated based on the total plastic volumetric strain and stress state, and these are stored for use in the next step.

2.2 Testing of Implementation and Validation

In the FY2013 milestone report (Davis et al. 2013) we presented some initial testing of the implementation by modeling drying and wetting cycles as typically observed in laboratory data. Here we present new modeling of a laboratory experiment of Pousada (1982) to test and demonstrate the capability of the implemented dual-structure model. In the laboratory experiment of Pousada (1982), an expansive clay undergoes several suction (wetting-drying) cycles for two net mean stresses (Figures 2.3 and 2.4). Expansive clays show irreversible behavior when they undergo successive wetting-drying cycles. This phenomenon cannot be reproduced with the standard single-structure BBM model, but the incorporation of the interactions between the microstructure and the macrostructure of an expansive soil allows accumulating plastic strain upon suction cycles. Table 2.1 shows the parameters of the dual-structure model resulting from the calibration of the laboratory experiments of Pousada (1982).

Table 2.1. Parameters used to reproduce the suction cycles test of Pousada (1982).

Parameters defining the Barcelona Basic Model for macrostructural behavior

κ_{Ps0} =0.005 κ_{sp0} =0.01 λ_{Ps0} =0.024 p^c (MPa)=0.01 r =0.85 ξ (MPa^{-1})=0.2 p_0^* (MPa)=0.75

Parameters defining the law for microstructural behavior

α_m (MPa^{-1})=1.2 β_m (MPa^{-1})=0.02

Interaction functions between the microstructure and the macrostructure

$f_c = 1.975 + 0.185 \tanh\left[5\left(p / p_0 - 0.275\right)\right]$ $f_s = 1.825 - 0.4 \tanh\left[-0.4\left(p / p_0 - 0.3\right)\right]$

e_{micro}=0.45 e_{macro}=0.55

Figure 2.3 shows the calibration of a suction-cycles test, which comprises five suction cycles (suction ranges from 1.7 to 0.2 MPa in each suction cycle) at a very low net mean stress (0.01 MPa). The model can reproduce the plastic strain accumulation upon cycles and the tendency to reduce the amount of plastic strain accumulated between two successive suction cycles as cycles accumulate. The calibration of the experiment reproduces with a fair accuracy the end points of the wetting-drying cycles, as well as the strain evolution of the first suction cycle, which is curved. Nevertheless, the strain evolution of the subsequent cycles becomes quite linear in the laboratory experiment, but the numerical results maintain the curved evolution. To improve this change in the strain evolution pattern as suction cycles evolve, a more complex bulk modulus for both the microstructure and macrostructure may need to be implemented.

While the microstructure behaves elastically (Figure 2.3b), the macrostructure undergoes plastic strain that causes irreversible changes in macroporosity, which is related to the macrostructural void ratio through $\phi_M = e_M / (1 + e)$ (Figure 2.3c). Macroporosity is enhanced at low net mean stress (low values of the p/p_0 ratio) as a result of the interaction between the two levels of structures. Low values of the p/p_0 ratio imply a dense macrostructure, so the swelling of the microstructure will open up the macrostructure, inducing expansion upon suction cycles. Thus, the plastic strain of the macrostructure

induced by the elastic volumetric strain of the microstructure is higher during wetting than during drying (Figure 2.3d).

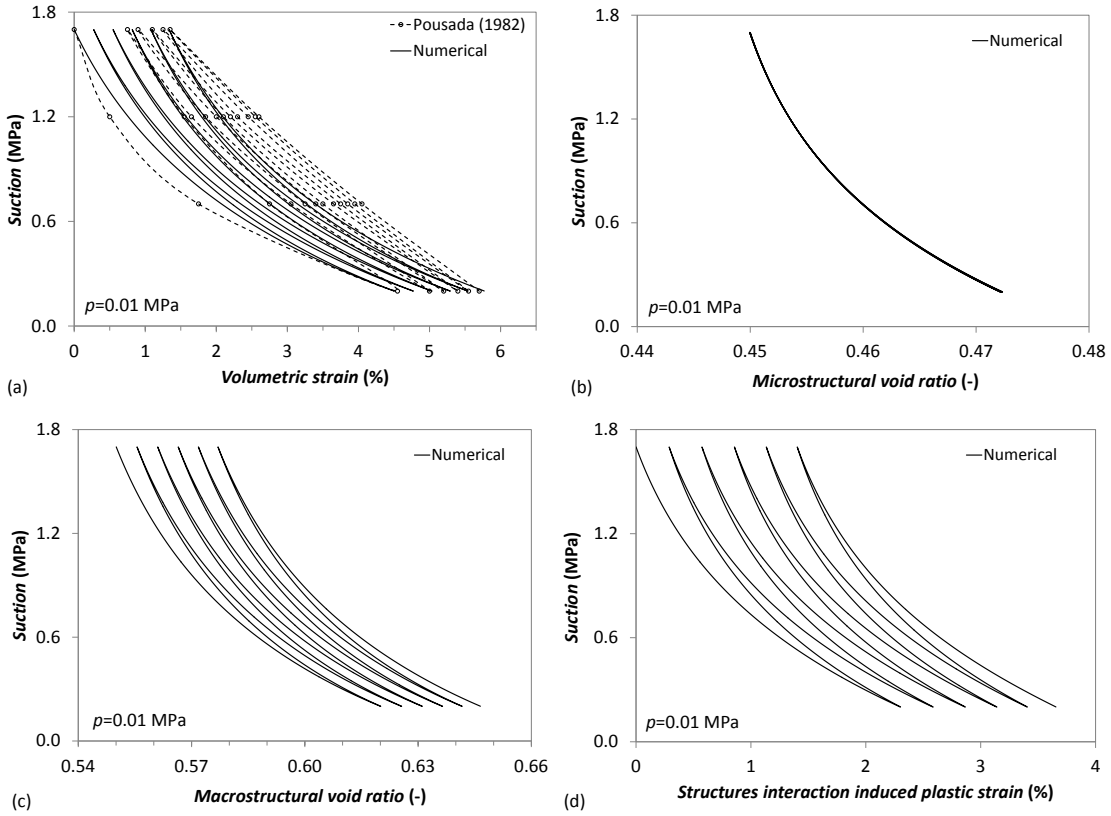

Figure 2.3. Evolution of (a) volumetric strain, (b) microstructural void ratio, (c) macrostructural void ratio and (d) plastic strain of the macrostructure due to micro/macrostructure interaction upon suction (wetting-drying) cycles for a net mean stress of 0.01 MPa. The experimental volumetric deformation of Pousada (1982) is also displayed in (a).

Figure 2.4 displays the results of the same experiment, but performed at a higher net mean stress of 0.1 MPa. Similarly to the experiment with a lower confining pressure, the numerical calibration reproduces fairly well the end points of the wetting-drying cycles and the curved strain evolution of the first cycle. But for subsequent suction cycles, the experimental strain evolution becomes quasi-linear, while the numerical simulation keeps the curved evolution. Comparing Figures 2.3 and 2.4 reveals that the swelling capacity of the material is reduced as the confining stress increases. The rest of the characteristics remain the same: the microstructure is elastic, plastic strain accumulation is reduced with the number of cycles, and expansion accumulates upon cycles. The latter occurs because the p/p_0 ratio is still relatively low and therefore, the macrostructure is dense. For a net mean stress that would yield a high p/p_0 ratio, the macrostructure would be loose and the microstructure would invade macropores upon suction cycles. In this case, given the net mean stress and suction values, the microstructure deformation is almost independent of the confining stress (recall Figures 2.3b and 2.4b), because its stiffness is proportional to the effective stress (Equation (2.13)), which evolves very similarly in the two experiments. Apart from this, the higher net mean stress of 0.1 MPa (Figure 2.4) implies a higher p/p_0 ratio, and therefore the suction cycles are closer to the equilibrium point between the wetting and the drying interaction functions.

This causes a smaller plastic strain accumulation upon suction cycles due to the interaction between the two structural levels (compare Figures 2.3d and 2.4d).

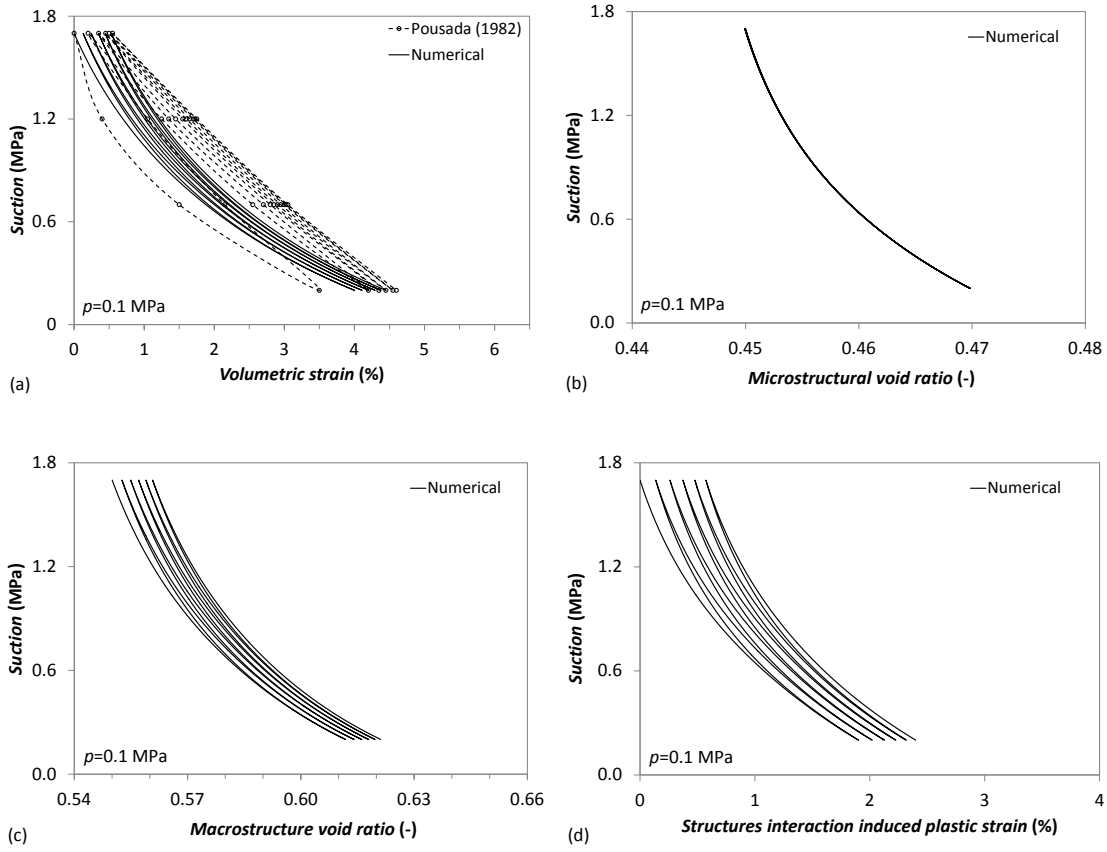

Figure 2.4. Evolution of (a) volumetric strain, (b) microstructural void ratio, (c) macrostructural void ratio and (d) plastic strain of the macrostructure due to micro/macrostructure interaction upon suction (wetting-drying) cycles for a net mean stress of 0.1 MPa. The experimental volumetric deformation of Pousada (1982) is also displayed in (a).

The calibration of the dual-structure model with only these two available experiments becomes quite complicated, due to the large number of degrees of freedom that this model has. Though the simulated deformation paths differ somewhat from the experimental results, the global behavior of this expansive clay is satisfactorily captured. In general, more experiments would be required to back-calculate most of the parameters of the dual-structure model.

2.3 Application to a Generic Repository

We applied the dual-structure model and compared the THM results with those of the standard single-structure BBM in a generic repository similar to that considered in the Swiss nuclear waste disposal program. We assume that the host rock is Opalinus Clay. The tunnels containing the high-level waste are placed at 500 m depth and are spaced 50 m. Since the emplacement tunnels may typically be up to 1 km long, we model a 2D cross section of the repository and make use of the symmetry to model only one

tunnel. We further assume that the tunnel is backfilled with FEBEX bentonite (Gens et al. 2009; Sánchez et al. 2012). The geometry of the model and the heat load of the waste are displayed in Figure 2.5.

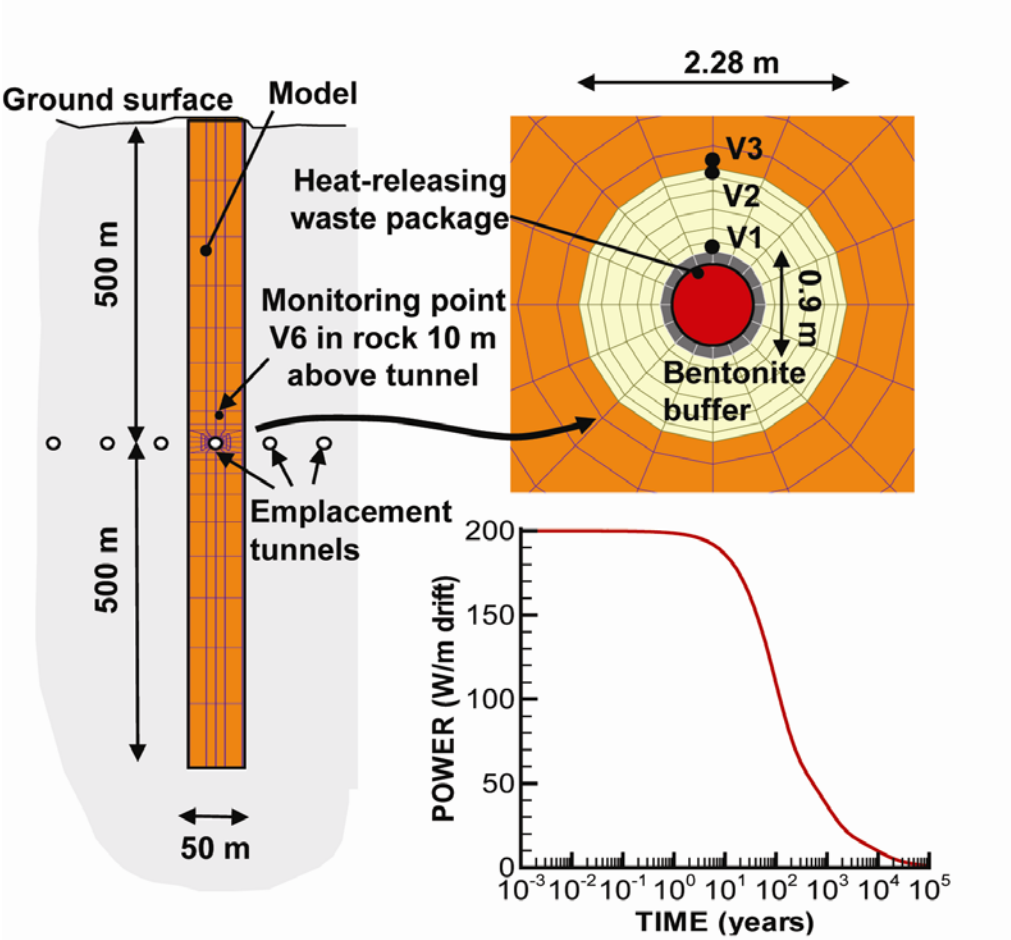

Figure 2.5. Model domain, numerical grid, monitoring points and heat power function for an assumed bentonite back-filled horizontal emplacement drift at 500 m depth in clay host rock.

Table 2.2 compiles the material parameters of the claystone host rock. The properties of the Opalinus Clay are taken from Gens et al. (2007) and Corkum and Martin (2007). The relative permeability curves follow the van Genuchten-Mualem model. The properties of the FEBEX bentonite for the standard single-structure BBM model were derived by Alonso et al. (2005) and Gens et al. (2009) (Table 2.3) and were also used in Rutqvist et al. (2014). The properties for the macrostructure of the dual-structure model are similar to those used in the single-structure BBM model, but some parameters have been adapted to obtain a global behavior of both the microstructure and the macrostructure comparable to that of the BBM model (see Table 2.4). The properties of the microstructure of the dual-structure model for the FEBEX bentonite are based on those proposed by Sánchez et al. (2012), but with some modifications (Table 2.4).

Table 2.2. Properties of the clay host rock (Gens et al., 2007; Corkum and Martin, 2007).

Property	Value
Porosity, ϕ (-)	0.15
Young's modulus, E (GPa)	5
Poisson ratio, ν (-)	0.3
Grain density, ρ_s (kg/m^3)	2400
Grain Specific heat, C_s (J/kg/ºC)	900
Thermal conductivity, λ_T (W/m/K)	2.2
Thermal expansion coefficient, α_0 (ºC^{-1})	1.0x10^{-5}
Intrinsic permeability, k (m^2)	5.0x10^{-20}
van Genuchten water retention parameter *m* (-)	0.41
van Genuchten entry pressure, P_0 (MPa)	48
Residual liquid saturation, S_{lr} (-)	0.1
Residual gas saturation, S_{gr} (-)	0.01

Table 2.3. Material parameter values for the bentonite buffer used in the BBM model (Gens et al., 2009).

Property	Value
Initial dry density, ρ_d (kg/m^3)	1600
Compressibility parameter for stress-induced elastic strain, κ_{Ps0} (-)	0.05
Compressibility parameter for suction-induced elastic strain, κ_{sp0} (-)	0.25
Poisson ratio, ν (-)	0.4
Parameter for stress-induced elastic strain, α_{ps} (MPa^{-1})	-0.003
Parameter for suction-induced elastic strain, α_{sp} (-)	-0.161
Parameter for suction-induced elastic strain, α_{ss} (-)	0
Reference stress state for relating elastic compressibility to suction, p_{ref} (MPa)	0.01
Thermal expansion coefficient, α_0 (^{o}C^{-1})	1.5x10^{-5}
Compressibility parameter in virgin state soils at zero suction, λ_{Ps0} (-)	0.15
Parameter defining soil stiffness associated with loading collapse yield, r (-)	0.925
Parameter for the increase of soil stiffness with suction, ξ (MPa^{-1})	0.1
Parameter that describes the increase of cohesion with suction, k_s (-)	0.1
A reference stress state for compressibility relation in virgin states, p^c (MPa)	0.5
Slope of the critical state line, M (-)	1.0
Non-associativity parameter in the plasticity flow rule, α_a (-)	0.53
Specific volume at reference stress state p^c in virgin state, v^c (-)	1.937
Net mean yield stress for saturated conditions at reference temperature, p_0^* (MPa)	12.0
Initial porosity, ϕ_0 (-)	0.398
Saturated reference permeability at reference porosity ϕ_0, k_0 (m^2)	4.5x10^{-27}
Reference porosity for the permeability model, ϕ_0 (-)	0.14
Model parameter for permeability, b (-)	50
Relative permeability to liquid, k_{rl} (-)	$k_{rl} = S_l^3$
Relative permeability to gas, k_{rg} (-)	$k_{rg} = 1$
Klinkenberg parameter, b_k (MPa)	2.5x10^5
van Genuchten water retention parameter *m* (-)	0.32
van Genuchten entry pressure, P_0 (MPa)	30
Residual liquid saturation, S_{lr} (-)	0.1
Residual gas saturation, S_{gr} (-)	0
Grain Specific heat, C_s (J/kg/^{o}C)	800
Thermal conductivity, λ_T (W/m/K)	$0.5 + S_l(1.3 - 0.5)$

Table 2.4. Material parameter values of the bentonite buffer used in the dual-structure model (only the parameters of the macrostructure that differ from those used for the BBM model (Table 2.3) are included here) (Sánchez et al., 2012).

Property	Value
Compressibility parameter for stress-induced elastic strain, κ_{Ps0} (-)	0.079
Compressibility parameter for suction-induced elastic strain, κ_{sp0} (-)	0.08
Reference stress state for relating elastic compressibility to suction, p_{ref} (MPa)	0.03
Specific volume at reference stress state p^c in virgin state, v^c (-)	1.4935
Initial void ratio of the macrostructure, e_M (-)	0.35
Initial void ratio of the microstructure, e_m (-)	0.3
Parameter controlling the microstructural soil stiffness, α_m (MPa^{-1})	0.006
Parameter controlling the microstructural soil stiffness, β_m (MPa^{-1})	0.0027
Interaction function for microstructural swelling paths	$f_s = 0.8 - 1.1\tanh\left[20\left(p/p_0 - 0.25\right)\right]$
Interaction function for microstructural compression paths	$f_c = 1.0 + 0.9\tanh\left[20\left(p/p_0 - 0.25\right)\right]$
Saturated reference permeability at reference porosity ϕ_0, k_0 (m^2)	3.0x10^{-23}
Reference porosity of the macrostructure for the permeability model, ϕ_{M0} (-)	0.14

We assume that the intrinsic permeability varies according to an exponential law that was proposed and calibrated against laboratory measurements by Sánchez et al. (2012) for the dual-structure model. This law depends on the porosity of the macrostructure as

$$\mathbf{k} = k_0 \exp\left[b\left(\phi_M - \phi_{M0}\right)\right]\mathbf{I}, \tag{2.21}$$

where $\mathbf{k}$ is the intrinsic permeability tensor, k_0 is the intrinsic permeability at the reference porosity of the macrostructure ϕ_{M0}, b is a model parameter and $\mathbf{I}$ is the identity matrix. For the single-structure BBM model, we adopt the same law, but change macroporosity to total porosity and adjust the value of k_0, so that the initial permeability is the same in the two cases (2.0×10^{-21} m^2). Furthermore, to account for the higher intrinsic permeability of clays to gas than to water (Olivella and Gens, 2000), we make use of the relationship given by Klinkenberg (1941)

$$\mathbf{k}_{gas} = \mathbf{k}\left(1 + \frac{b_k}{p_g}\right), \tag{2.22}$$

where b_k is the Klinkenberg parameter.

To calculate consistent initial conditions of the repository once the emplacement tunnel has been excavated and the backfill and the waste placed inside the tunnel, we calculate a sequence of stages. First, we calculate the pre-excavation equilibrium conditions. Mechanically, we assume that the stress field is isotropic and the vertical total stress increases linearly with depth and proportionally to a bulk density of 24 kN/m^3. Since the tunnel is located at 500 m depth, the pre-excavation mean stress is 11.8 MPa. The mechanical boundary conditions are no displacement perpendicular to the lateral and bottom boundaries

and a constant pressure equal to atmospheric pressure at the upper boundary. Hydraulically, the groundwater table is located at the ground surface. Fluid pressure is imposed at the bottom of the model, at 1000 m depth, and is set to 9 MPa. The ground surface temperature and the temperature at the bottom of the model are fixed to 10ºC and 40ºC, respectively. Thus, the geothermal gradient is equal to 30ºC/km. Next, we simulate the drift excavation by removing the elements in the tunnel and fixing the temperature at 25ºC and the fluid pressure at 0.1 MPa until steady state is reached. Finally, the nuclear waste canister and the bentonite buffer are placed in the tunnel instantaneously, and the waste starts to release heat. The bentonite has an initial liquid degree of saturation of 0.65 and an initial gas pressure of 0.1 MPa.

Figure 2.6 shows the evolution of temperature, liquid saturation degree, liquid pressure, and total mean stress at some points within the buffer and in the Opalinus Clay, obtained with both the BBM and the dual-structure model. Temperature evolution is similar for both mechanical constitutive models, though the temperature peak is slightly higher close to the canister for the dual-structure model, because the buffer becomes drier than for the standard single-structure BBM (Figure 2.6a). However, the hydration of the buffer is significantly affected by the mechanical constitutive model (Figure 2.6b). While the buffer close to the canister becomes fully saturated after 60 years for the BBM, it takes up to 2780 years when using the dual-structure model. Though the exact time at which the buffer will become fully saturated is very uncertain (because we do not know with precision all the parameters of the dual-structure model), the difference of two orders of magnitude between the saturation time predicted by the BBM and the dual-structure model shows the importance of using a constitutive model, which accounts for two structural levels to reproduce the thermo-hydro-mechanical behavior of expansive clays. This difference in the saturation time of the buffer occurs because in the dual-structure model, the porosity through which fluid flow occurs is limited to the porosity of the macrostructure and not the total porosity, as in the BBM. The deviation in the saturation evolution in the inner part of the buffer between the two models starts at early times (2–3 years), which is in agreement with the observations of the 10-year-long mock-up test for the FEBEX *in situ* test performed at the laboratory at CIEMAT, Madrid (Spain) (Sánchez et al. 2012). Furthermore, the delay in the saturation of the bentonite buffer causes a delay in its pressurization close to the canister (Figure 2.6c). Despite this significant delay in saturation at the inner parts of the buffer, the overall buffer swelling stress evolution is not severely retarded (Figure 2.6d). Indeed, the buffer is still functioning to provide sufficient swelling and support load to the tunnel wall and the EDZ (Figure 2.7).

Figure 2.8 displays the variables that control the dual-structure constitutive model, i.e., suction, mean net stress and effective stress. While suction and mean net stress are used to calculate the behavior of the macrostructure according to the BBM, the mean effective stress determines the elastic volumetric strain of the microstructure in the dual-structure model. Suction close to the tunnel wall decreases from the beginning of the simulation, because the host rock, which is fully saturated, supplies groundwater that gradually saturates the bentonite buffer (Figure 2.8a). However, suction initially increases close to the canister because the heat of the high-level nuclear waste dries the bentonite. Subsequently, the saturation of the entire bentonite buffer starts to take place, and suction decreases. The net mean stress (Figure 2.8b) is similar for both models close to the tunnel wall, because of the relatively quick saturation of this part of the buffer, which leads to a comparable high stiffness of the expansive clay (Figure 2.8d). However, close to the canister, the net mean stress becomes much higher for the dual-structure model than for the BBM, because the higher suction (recall Figure 2.8a) leads to a stiffer bentonite (Figure 2.8d). The effective mean stress evolution (Figure 2.8c) is similar to the suction evolution because the net mean stress is relatively low.

Figure 2.9 illustrates porosity evolution for simulation results of both constitutive models. The total porosity changes, though larger in the dual-structure model, are relatively similar for both models, especially in the region of the buffer close to the tunnel wall. However, a higher porosity reduction occurs close to the waste overpack, where a stronger drying takes place when accounting for the dual-structure model. Interestingly, the reduction in macroporosity is larger than the reduction in total porosity close to

the waste overpack. This larger macroporosity reduction in the dual-structure model leads to a greater permeability reduction close to the waste overpack that impedes hydration of the buffer (Figure 2.10).

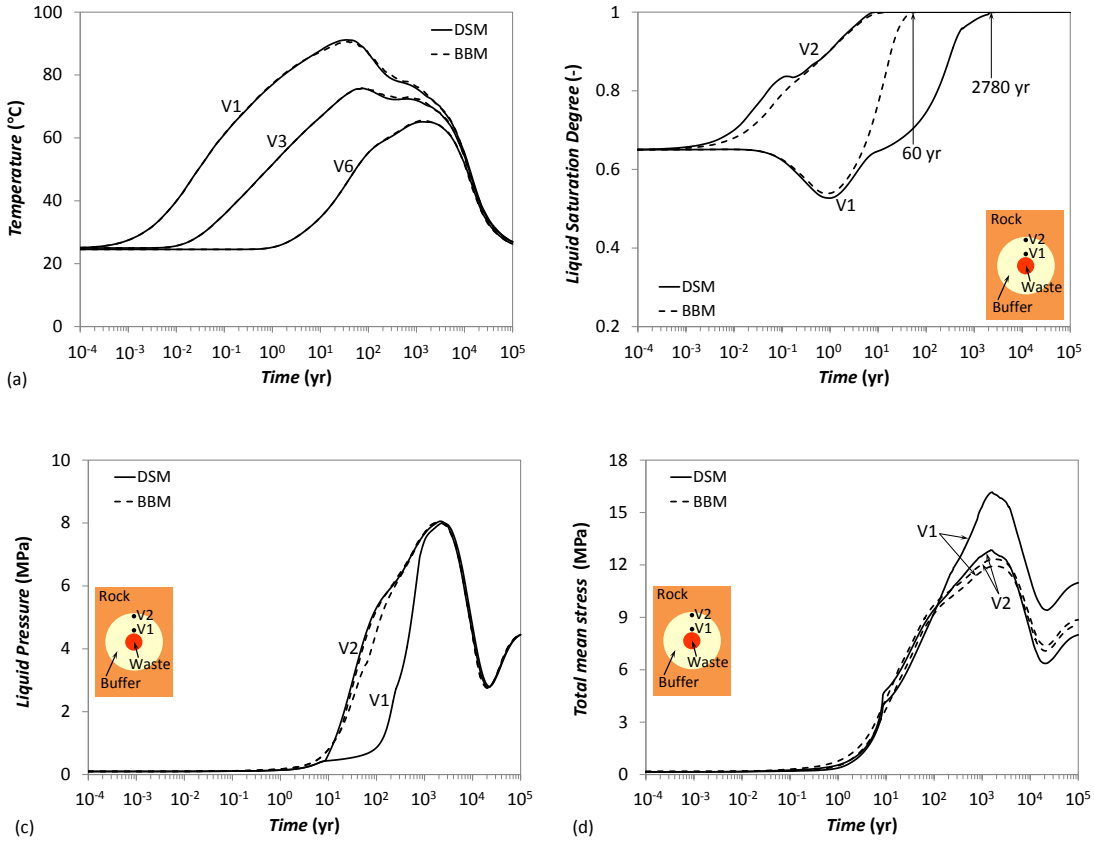

Figure 2.6. Evolution of (a) temperature (see Figure 2.5 for the location of the observation points), (b) liquid saturation degree, (c) liquid pressure and (d) total mean stress for the dual-structure model (DSM) and the standard single-structure Barcelona Basic Model (BBM).

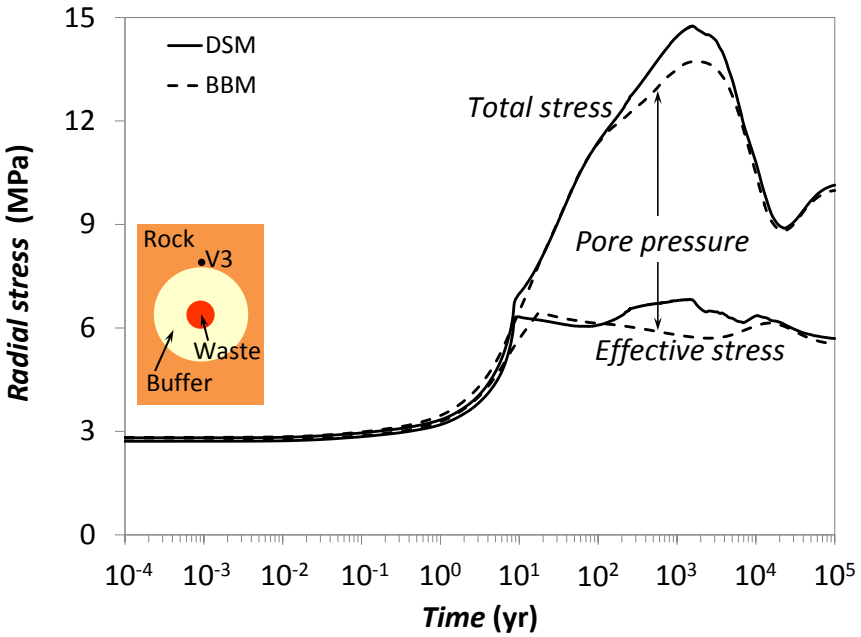

Figure 2.7. Evolution of the total and effective radial stress at point V3 located at the tunnel wall for the dual-structure model (DSM) and the standard single-structure Barcelona Basic Model (BBM).

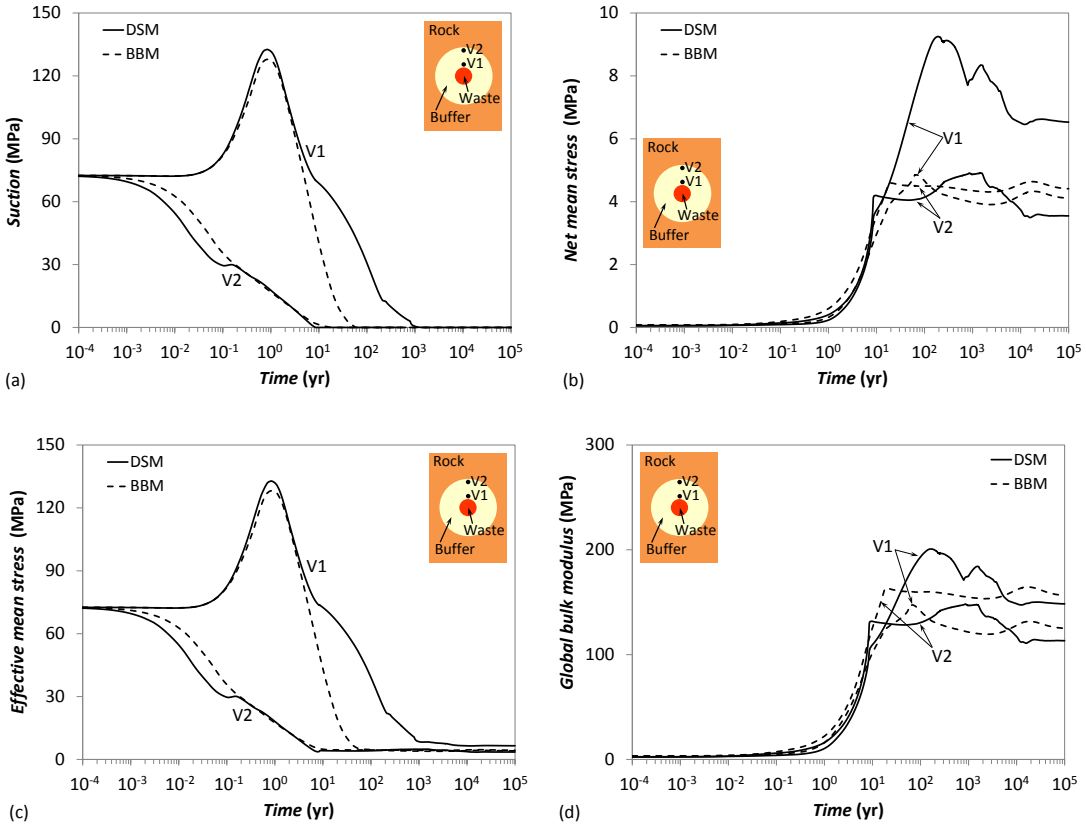

Figure 2.8. Evolution of (a) suction, (b) net mean stress, (c) effective mean stress and (d) global bulk modulus for the dual-structure model (DSM) and the standard single-structure Barcelona Basic Model (BBM).

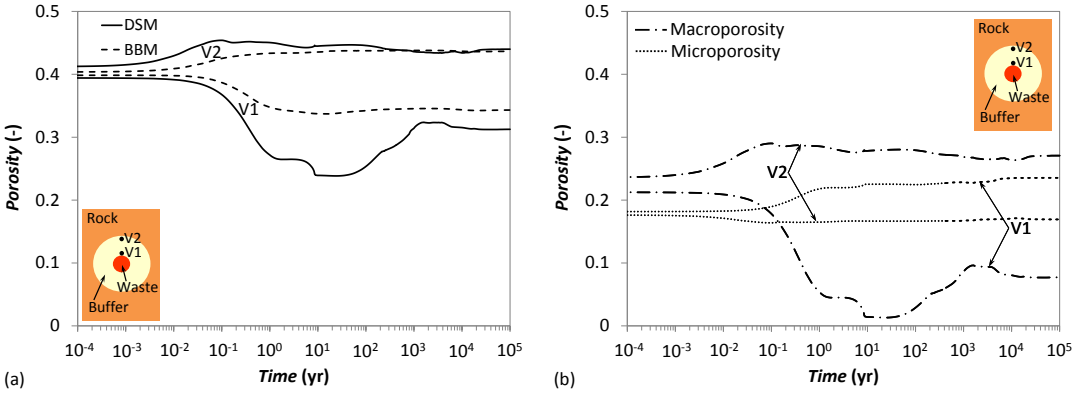

Figure 2.9. (a) Total porosity evolution for the dual-structure model (DSM) and the standard single-structure Barcelona Basic Model (BBM). (b) Macroporosity and microporosity evolution of the dual-structure model.

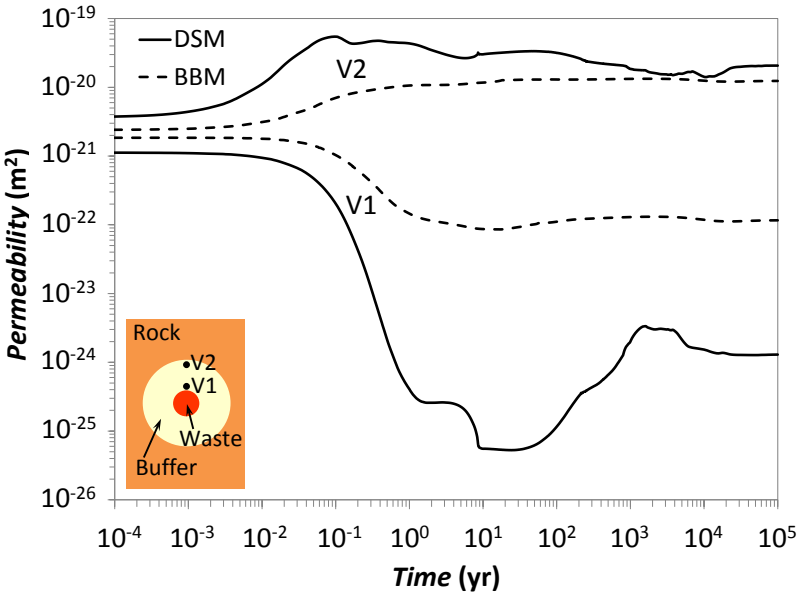

Figure 2.10. Permeability evolution for the dual-structure model (DSM) and the standard single-structure Barcelona Basic Model (BBM). Permeability is a function of the macroporosity in the dual-structure model.

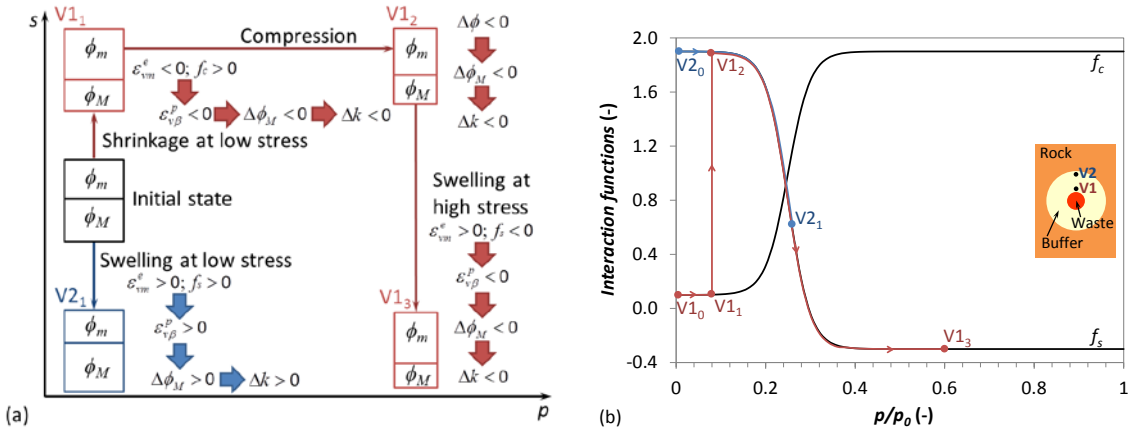

Figure 2.11. (a) Schematic evolution of the microporosity, macroporosity, plastic strain of the macrostructure due to micro/macrostructure interaction and permeability and (b) evolution of the interaction functions for a point close to the canister (V1) and a point close to the tunnel wall (V2).

Figure 2.11 schematically illustrates the evolution of the microporosity and the macroporosity at a point close to the canister and at another point close to the tunnel wall. The expansive clay close to the tunnel wall becomes saturated at a low mean stress. Thus, both the microstructure and the macrostructure swell (strain is positive) and since the interaction function of swelling at low stress is positive (Figure 2.11b), the plastic strain of the macrostructure due to interaction between the two structural levels is positive, i.e., the macrostructure expands (Figure 2.11a). Therefore, the permeability of the clay increases and full saturation occurs relatively quickly. On the other hand, close to the canister, the buffer dries during the first year of simulation, leading to shrinkage at low stress (strain is negative). In this case, since the interaction function of shrinkage at low stress is positive, the plastic strain of the macrostructure due to interaction between the two structural levels is negative, which implies shrinkage of the macrostructure and therefore, a permeability reduction. Later, the permeability is reduced even further because the mean stress of the buffer increases, which causes a compression of the pores. Finally, the region around the canister is saturated at high stress. Under these conditions, the microstructure swells (strain is positive), but the interaction function of swelling at high stress is negative (Figure 2.11b). As a result, the plastic strain of the macrostructure due to interaction between the two structural levels is negative, i.e., the macrostructure shrinks. This shrinkage of the macrostructure is caused by an invasion of the microstructure, which closes the macropores when the expansive clay swells at high stress, contributing to reduce the permeability. This greater permeability reduction around the waste overpack when using the dual-structure model causes a significant delay in the time at which the buffer becomes fully saturated. These results are in agreement with those of Sánchez et al. (2012), who modeled a large-scale heating test—a mock-up test that lasted for 10 years for the FEBEX *in situ* test—performed in the laboratory. Their modeling results reproduce the experimentally observed delay of the saturation of the buffer in the short-term when using the dual-structure model instead of the BBM. In our study, we show how such a delay might affect the long-term THM evolution of a repository.

2.4 Coupled CM coupling through dual-structure model

To date we have considered and applied several CM coupling approaches, including an empirical model wherein we consider swelling stress caused by changes in ionic concentration and smectite volume fraction, and another approach in which the microstructural strain in the dual-structure model depends on the concentration of each exchangeable cation. The first model has been applied to simulate the effects of

illitization on swelling pressure at high temperatures. This work and simulation results are presented in the upcoming FY2014 milestone report "Investigation of Coupled Processes and Impact of High Temperature Limits in Argillite Rock." The second approach wherein microstructural strain is dependent on each exchangeable cation concentration was already demonstrated in a TOUGHREACT-FLAC modeling example presented in the FY2013 milestone report. In this report, the effect of ionic strength (or total ion concentration) on bentonite swelling and abundance of smectite has been implemented into the dual-structure model. The mathematical formulations for CM coupling are summarized below.

When CM coupling is considered, the dependence of microstructural volumetric strain on the change in the microstructural effective stress,

$$\mathrm{d}\varepsilon_{vm}^{e} = \frac{f_s}{K_m}\mathrm{d}\hat{p}\,, \tag{2.23}$$

where $\hat{p} = p + s_m$, p is the effective mean stress; and s_m is the microstructural suction. f_s is the mass fraction of smectite in bentonite. K_m is given in Equations (2.13a and 2.13b). s_m has two components, matric suction, s, and osmotic suction, s_o, i.e. $s_m = s + s_o$. The effect of ionic strength of the pore water on microstructural strain is carried out via the osmotic suction, which is computed as:

$$s_o = -10^{-6}\frac{RT}{V_w}\ln(a_w)\,, \tag{2.24}$$

where V_w is the molar volume of water (in m^3/mol), and a_w is the activity of water. a_w is calculated in TOUGHREACT (Xu et al. 2011) as follows,

$$\ln(a_w) = -\Phi m^* \frac{1}{55.51}, \tag{2.25}$$

where Φ is osmotic coefficient of the solution and m^* is the sum of the molalities of all species in solution.

The effect of exchangeable cations is linked to mechanics through the dependence of β_m (see Equation 2.24) on exchangeable cation concentration as shown in the following equation (Gens 2010):

$$\beta_m = \sum_i \beta_m^i x_i\,, \tag{2.26}$$

where x_i is the equivalent fraction of the exchangeable cation, i, ranging from 0 to 1, and β_m^i is the parameters that control the microstructure stiffness and defined for each of the exchangeable cations.

As shown in Equation (2.24), the larger the β_m, the more soil swells, and the soil is softer. Gens (2010) and Guimarães et al. (2013) proposed that β_m^i is proportional to the ionic hydrated radius and inversely proportional to its valence, and typically $\beta_m^{Li} > \beta_m^{Na} > \beta_m^{K}$ and $\beta_m^{monovalent} > \beta_m^{bivalent}$. If this is true, one could infer that Na-smectite which contains exclusively Na in the interlayer space should swell more than Ca-smectite, provided that other conditions are the same. However, experimental results seem to be controversial.

Likos and Wayllace (2010) reported that "Water uptake, volume change, and swelling pressure were all more significant for Colorado (Ca^{2+}/Mg^{2+}) bentonite than for Wyoming (Na^{+}) bentonite." Their results

seem to support that Ca-Mg smectite exhibits more swelling than Na smectite. However, when two different types of bentonite are compared, material compositional differences between the bentonites can impact the results. Note that exchangeable cations in Colorado bentonite are dominated by Ca and Mg with 59% Ca and 38% Mg, whereas exchangeable cations in Wyoming bentonite are composed of 59% Na, 36% Ca and 5% Mg—Wyoming bentonite still contains a considerable amount of exchangeable Ca. Several facts have to be considered when the study by Likos and Wayllace (2010) is used as an example that Ca-Mg smectite exhibits more swelling than Na smectite. First, Colorado bentonite contains more smectite (90%) than Wyoming bentonite (70–90%). Second, in the free-swelling test, the Colorado bentonite is not compacted to the same density as Wyoming bentonite. As shown in Figure 2.12 (the same as Figure 4 in Likos and Wayllace 2010), Colorado bentonite has an initial porosity ratio of 0.83, whereas Wyoming bentonite has an initial porosity ratio of 0.88. Because the higher degree of compaction (higher density) leads to the larger strain, the difference in initial density contributes the higher swelling of Colorado bentonite. Third, the comparison between Ca-exchanged Wyoming bentonite and untreated Wyoming bentonite reflects the effect of exchangeable cations on the swelling. Both samples have the same density, but one is 59% Na (untreated) and another is supposed to have 100% Ca. However, as shown in Figure 2.12(c), Ca-exchanged Wyoming bentonite actually swells less than untreated Wyoming bentonite.

Ironically, it is very well known that Na-smectite swells more than Ca-smectite. Mitchell and Soga (2005) state that “sodium and lithium montmorillonite may undergo almost unrestricted interlayer swelling provided water is available, the confining pressure is small, and the electrolyte concentration is low. On the other hand, divalent and trivalent forms of montmorillonite do not expand beyond a basal spacing of about 17 Å and form multi-particle clusters or aggregates, regardless of other environmental factors.”

To support the negative correlation of β_m with the valence of exchange cations, Guimarães et al. (2013) cited the work by Sridharan et al. (1986), who conducted a series of one-dimensional consolidation tests with homoionized bentonite. The initial moisture contents of samples are approximately 50% of the liquid limit. Since the Na-smectite has much higher liquid limit than Ca-smectite, the initial water content for different homoionized bentonite are very different, e.g., 257% for Na-bentonite and 89% for Ca-bentonite. As a result, the initial void ratios are different. To obtain a compressibility curve starting from the same point, the total compression at the end of each load increment (δ) is divided by the height of the soil solid (H_s as a percentage). Figure 2.13 (the same as Figure 4 in Sridharan et al. 1986) clearly shows that monovalence ions lead to more swelling than bivalence ions.

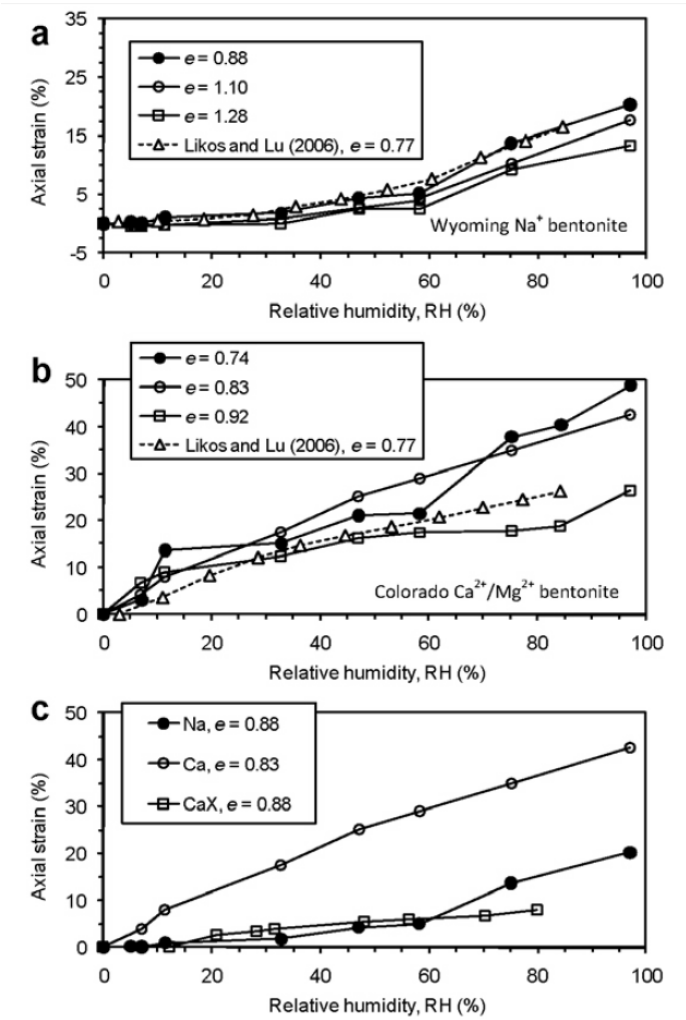

Figure 2.12. Axial-strain response measured along hydration paths under free swelling conditions: (a) Wyoming bentonite, (b) Colorado bentonite, (c) Wyoming, Colorado, and Ca^{2+}-exchanged Wyoming bentonite (denoted CaX) (the same as Figure 4 in Likos and Wayllace 2010).

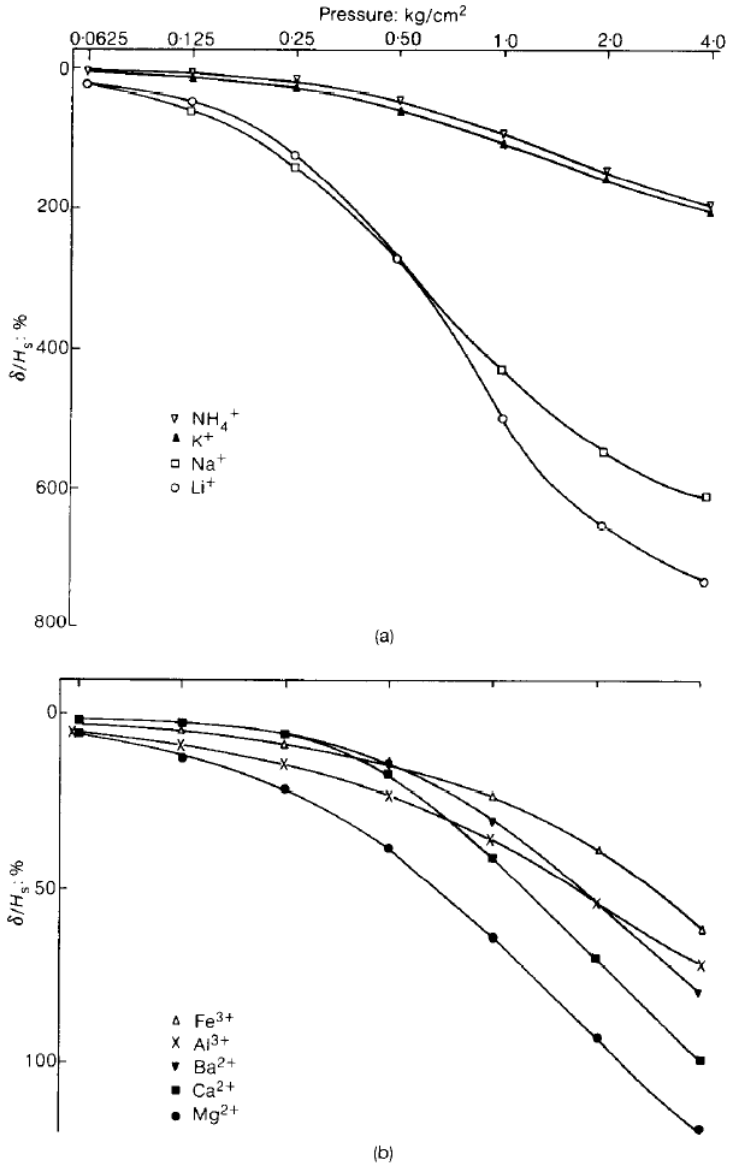

Figure 2.13. Percentage compression-pressure plots: (a) for monovalent bentonites; (b) for divalent and trivalent bentonites (Sridharan et al. 1986).

Similar experiments were also conducted in Di Maio (1996; 1998). In a series of conventional oedometer tests with Ponza bentonite (mainly composed of Na-smectite) having initial water content close to the liquid limit, specimens were exposed to saturated solutions (NaCl, KCl, and $CaCl_2$) with different concentrations. Then the void ratio versus effective stress and the volumetric strain change with time were measured. The following observations are fairly clear from the compression of saturated bentonite samples: (1) bentonite with higher valence cations has a low liquid limit and plastic limit, which is very well known by the soil mechanics community. Likos and Wayllace (2010) even use this as a confirmation of whether the bentonite is Ca-Mg bentonite or Na-bentonite. It is also known that the more plastic the mineral, the more potential swelling and shrinkage (see p. 103 in Mitchell and Soga, 2005). So qualitatively, it seems that bentonite with higher valence cations has a lower swelling potential than bentonite with monovalence (but K^+ might be an outlier).

After examining the published data, we propose the following equation to estimate β_m^i:

$$\beta_m^i = \kappa r^i / v^i, \tag{2.27}$$

where κ is a constant that has to be calibrated and r^i is hydrated radii of the cation and v^i is the valence of the cation. Equations (2.22) to (2.27) have been implemented in TOUGHREACT-FLAC and further testing will be conducted in the future.

The CM coupling through the dual-structure model represents the microscopic physical and chemical processes related to the swelling of bentonite. Therefore, it is likely to provide a more accurate prediction of the swelling behavior of bentonite under simultaneous heating, hydration, and chemical alteration as undergone by the EBS bentonite in a typical repository. However, validating such CM coupling by experimental data is quite difficult, because there are few measurements. Experiments that can be used to validate the CM coupling should at least have the following conditions: (1) the dual-structure BExM has been used to calibrate the stress/strain evolution, (2) hydrological conditions are measured, and (3) chemical conditions, including both the aqueous solution and solid phase, must be known. Based on our recent current literature survey, no published experiments have been conducted that capture all of these aspects.

2.5 Conclusions

We are developing and applying coupled THMC models for the analysis of EBS coupled processes in bentonite-backfilled repositories. We base this development on the extension of the Barcelona Basic Model (BBM) to a dual-structure model for expansive clay, such as bentonite. We have implemented the dual-structure model into TOUGH-FLAC and have tested the model against literature data from experiments and independent models. We have shown the capabilities of the dual-structure model by modeling and reproducing observed behavior for two laboratory tests performed by Pousada (1982) on expansive clay under increasing confining stress. The simulations yielded irreversible strain accumulation upon suction cycles and a decreasing swelling capacity as the confining stress increases, in agreement with Pousada's (1982) laboratory observations.

We have completed model simulations of a generic high-level nuclear waste repository with waste emplacement in horizontal tunnels backfilled with expansive clay and hosted in a clay-rock formation. To our knowledge, this the first time a dual-structure model has been applied to model coupled THM processes of a repository over a 100,000-year time period. We compared the THM results of the dual-structure model with those of the standard single-structure BBM, showing the importance of considering the dual-structure behavior of the expansive soil material when modeling the THM behavior of a nuclear waste repository involving a protective bentonite buffer. The main difference between the two models is that the dual-structure model predicts that the time for full saturation of the expansive clay is on the order of thousands of years, while the BBM yields a time on the order of tens of years. The numerical simulation shows that this delay is caused by the fact that the fluid flow conducting macrostructure is invaded by the microstructure, with associated reduction in permeability for water flow. Such a delay has previously been observed in large-scale laboratory and *in situ* experiments; here we show this might affect the long-term performance of a repository. However, the modeling results also showed that despite a significant delay in saturation along the inner parts of the buffer, the overall buffer swelling stress evolution was not severely retarded. That is, the buffer is still functioning to provide sufficient swelling and support load to the tunnel wall and the EDZ.

We also upgraded the chemical and mechanical (CM) coupling scheme based on the dual-structure model for expansive clay. Now the microstructural swelling depends not only on the concentration of exchangeable cations, as implemented in FY2013 report (Davis et al., 2013), but also on the mass fraction of smectite and the ion concentration of pore water. This coupling scheme was implemented in coupled THMC code TOUGHREACT-FLAC3D, but it needs to be validated with experimental data, and its effect on the long-term THMC behavior of EBS bentonite will be evaluated through THMC models that adopt the dual-structure model and the upgraded CM coupling scheme in the future. Moreover, another CM coupling not considered to date is the effects of silica precipitation (cementation) on the mechanical behavior of the bentonite buffer. It is expected that cementation could make the buffer brittle, i.e., prone to fracturing when exposed the thermal stresses. This is another CM process that we will explore in the future.

3. ION ADSORPTION AND DIFFUSION IN SMECTITE CLAY BARRIERS

The long-term management of nuclear waste repositories requires reliable predictions of diffusion through waste-containment barriers, such as compacted bentonite. For clays, cation diffusion processes are influenced by: (1) the electrical charge of the diffusing solute, (2) the degree of compaction, and (3) the electrical double-layer structure at the clay/water interface. Most currently available diffusion models do not specifically include the expected changes in metal-diffusion rates due to these variations. A "de-coupling" of parameters and processes is necessary to ensure an accurate prediction of apparent diffusion rates under the chemical gradients expected within engineered barrier systems.

In order to achieve this goal, laboratory-scale diffusion experiments were performed, and in collaboration with colleagues, the data were described by reactive diffusive transport of calcium and bromide through lightly compacted montmorillonite.

3.1 Background

Smectite minerals are swelling clay minerals that have the form of flake-shaped particles, that are ubiquitous in soils and sedimentary environments, with a mica-like structure and characteristic dimensions on the order of 1 nm in thickness and ~200 nm in diameter (Tournassat et al. 2003). Because of their high specific surface area and cation exchange capacity, these natural "nano"-particles can strongly influence the geochemistry, mass-transfer properties, and mechanics of porous media in which they are present. For example, smectites play key roles in the isolation of landfills and high-level radioactive waste repositories (Altmann et al. 2012).

A recurrent theme in studies of the properties of smectite-rich media is the existence of strong couplings between their chemistry, mechanics, microstructure, and transport properties. These couplings are thought to arise because the pore width in clayey media is similar to the thickness of the electrical double layer (EDL), the interfacial region in which surface charge is screened by counter-ion adsorption and co-ion exclusion. According to the well-known Gouy-Chapman theory, the co-ion exclusion distance, a measure of the thickness of the EDL, equals twice the Debye length κ^{-1}, or about 6 nm and 2 nm at T = 298 K for a 1:1 electrolyte at ionic strengths (I) = 0.01 and 0.1, respectively, whereas a large number of the pores have a size of ~1 to 10 nm in clay shales and engineered clay barriers (Holmboe et al., 2012). Because of this similarity between pore width and EDL thickness, much of the pore water in smectite-rich media has properties distinct from those of bulk liquid water.

Current theories of the couplings between chemistry, transport, and mechanics in clayey media consistently use a conceptual model of overlapping EDLs in a single slit-shaped pore between parallel, uniformly-charged clay surfaces (Figure 3.1). Within this conceptual framework, a widely accepted model of the pore-scale details has yet to emerge The simplest models assume that all pores have the same width and that the EDL consists only of a diffuse ion swarm interacting with the surface through

long-range, nonspecific interactions. The resulting models have a single adjustable parameter, the geometric factor *G*. These simple models can qualitatively predict the coupled properties of compacted smectite clay barriers, but their quantitative agreement with experimental data is quite poor.

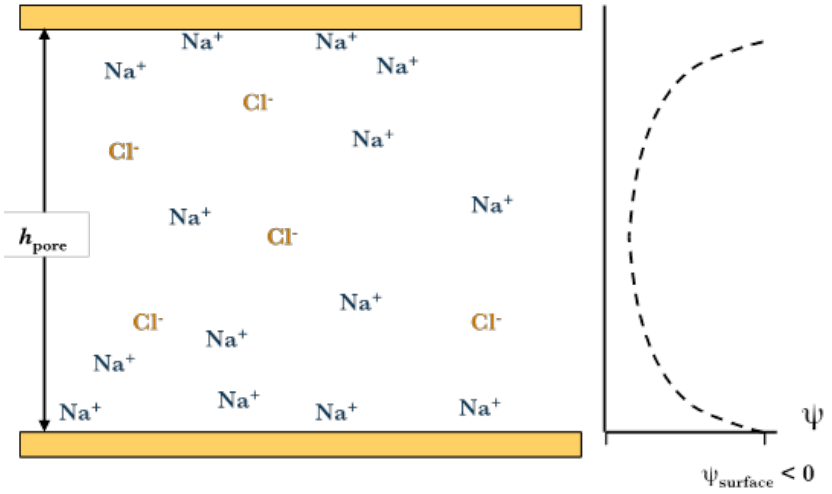

Figure 3.1. Pore-scale conceptual model used by models of coupled phenomena in compacted smectite clay barriers.

The persistence of very different models suggests that available macroscopic-scale data do not strongly constrain current theories of the properties of clay barriers. The present situation results from several challenges. The first challenge is that the microstructure of clay barriers is arduous to characterize with sufficient resolution to constrain existing models. X-ray diffraction techniques can detect the smallest pores present in smectite clay barriers (crystalline hydrates with a pore width of 0.3 to 0.9 nm) as well as some larger-scale features such as osmotic hydrates and interstratified stacking arrangements, but they provide limited information on larger-scale stacking arrangements, and they may be sensitive to sample preparation techniques. Electron microscopy techniques are not yet able to probe the microstructure of hydrated compacted clay on the length scale of the smallest pores, because of difficulties associated with beam damage and microstructural changes during sample drying. The second challenge is that the structure of the EDL in clayey media has never been directly observed: existing models are based on theoretical calculations, Monte Carlo simulations, and molecular dynamics (MD) simulations.

Despite these limitations, it is possible to test the plausibility of a series of pore models by carefully evaluating the physical meaning of their related fitting parameters on a single set of data. It must be noted that the many published models have not yet been benchmarked on a single and relevant set of data. In last year's EBS report, we presented new macroscopic-scale measurements of the adsorption and diffusion of trace levels of Ca^{2+}, Br^-, and HTO in a loosely compacted water-saturated Na-montmorillonite, a smectite mineral that is the main constituent of the bentonite used for engineered clay-barrier applications. In this report these data are modeled using a multicomponent reactive transport (diffusion) approach with various conceptual models to describe the electrical double layer, anion-accessible porosity, and other properties of interlayer pore structure. In addition, MD simulations are presented of adsorption and diffusion in individual clay interlayer nanopores, carried out under similar conditions (solid-liquid ratio, electrolyte composition) as the laboratory diffusion experiment. These results allow us to critically evaluate the ability of various EDL models to link molecular and macroscopic-scale adsorption and diffusion in compacted smectite.

Calcium was selected for the diffusion experiment in Na-montmorillonite, due to its relevance for U(VI) solution speciation and sorption behavior (Davis et al. 2013). Impurities of calcium minerals have to be

expected, both in the bentonite buffer as well as the bordering cement-based layer in engineered barrier systems. Hence, a calcium concentration gradient and the diffusive transport of Ca within barrier systems are very likely. At this point, only a few diffusion studies have been performed for Ca in bentonite; data for Ca diffusion in Na-montmorillonite is even more scarce (Kozaki et al. 2001). However, these data will be very relevant for the interpretation of uranium(VI) diffusion behavior in Na-montmorillonite at varying Ca concentrations. Furthermore, using calcium bromide as a salt allowed us to study the diffusion behavior of a fairly nonreactive anion (bromine) in a sodium chloride background electrolyte solution.

3.2 Experimental and modeling methods

3.2.1 Experimental

3.2.1.1 Materials

Acids, bases, and salt solutions used in experiments were of TraceSelect (Sigma Aldrich) or a comparable grade in order to minimize calcium background concentrations. Aqueous solutions were prepared with Nanopure water (Barnstead ultrapure water system).

A commercially available, well-characterized, standardized source clay (Na-montmorillonite, SWy-2, Clay Minerals Society) was selected in order to allow for a subsequent comparison with other data from the literature. The material is known to contain considerable amounts of impurities, such as quartz (8%), feldspars (16%), and calcite. The clay was pretreated to remove major mineral impurities, and to minimize a potential calcium release due to calcite dissolution during experiments.

3.2.1.2 Calcium bromide through-diffusion experiment

The calcium bromide through-diffusion experiment largely followed procedures previously described in detail in the literature (Molera and Eriksen 2002). The experimental setup consisted of the diffusion cell containing the clay packing, the high-concentration and low-concentration reservoirs, the tubings and fittings connecting the reservoirs with the diffusion cell, and a peristaltic pump. All solutions used in the experiment were repeatedly adjusted to pH 7 using small volumes of acid/base solutions (TraceSelect grade NaOH and HCl) prior to their contact with the mineral phase.

At the beginning of the experiment, a weighed aliquot of dry, Na-montmorillonite was packed into the "ring-like" component of the diffusion cell (PEEK, D=1.0 cm, L=0.5 cm) to give the desired dry density (~ 1.0 g/cm^3). The clay packing was contained between stainless-steel metal filters and carefully compacted with a custom-made PEEK rod. Then, high-concentration (200 mL) and low-concentration (20 mL) reservoirs were filled with background electrolyte solution (0.1 M NaCl, pH=7), and the clay was saturated with electrolyte by circulating the solutions through the cell with a peristaltic pump (0.7 mL/min) for about 4.5 weeks.

After clay saturation, the solution in the high-concentration reservoir was exchanged for a background electrolyte containing 1 mM $CaBr_2$, and the solution in the low-concentration reservoir was replaced with a 20 mL aliquot of fresh, $CaBr_2$-free electrolyte. Over the following weeks, the circulation of solutions through the diffusion cell was continued at the same flow rate. However, $CaBr_2$-free background electrolyte solutions in the low-concentration reservoir were continuously exchanged by replacing reservoir vials. This provided a nearly constant concentration gradient between high- and low-concentration reservoirs. The vials were weighed to correct for volume losses due to evaporation, sampled for Ca and Br analysis by IC and FIA analysis, respectively, and pH values were measured. Small volumes (1.5 mL) of the high-concentration reservoir solution were repeatedly sampled for Ca and Br analysis, in order to monitor solute concentrations and determine the concentration gradient over the course of the experiment. This procedure was continued until the diffusive fluxes for both Ca and Br reached steady-state conditions, and a series of data points were then collected at steady state.

After reaching steady-state conditions for Ca and Br diffusion, the solution in the high-concentration reservoir was replaced with a $CaBr_2$-free background electrolyte solution containing approximately 1000

Bq/mL (27 nCi/mL) of tritiated water (HTO). As before, low-concentration reservoir solutions were continuously replaced, and tritium activities analyzed by liquid scintillation counting until the diffusive flux of HTO had reached steady-state conditions.

3.2.1.3 Determination of anion-accessible porosity

Preliminary modeling results showed a difference between the diffusion-accessible porosity of packed Na-montmorillonite for tritiated water (HTO) and the anion (bromide). A separate experiment was conducted in order to experimentally determine the anion-accessible porosity. For this experiment, the same setup and procedures were used except that the diffusion cell was connected to two large (200 mL), high-concentration (0.1 M NaCl, 0.002 M NaBr) reservoirs at the beginning of the experiment. The background electrolyte (0.1 M NaCl, pH=7) and the bromide concentration (0.002 M Br as NaBr) were the same as in the through-diffusion experiment described above.

After equilibrating the clay with the reservoir solutions, the wet clay packing was extruded and dried at 150°C to determine its water content by weight difference and compute the exact dry density. After grinding the clay, bromide was extracted based on the procedure of Glaus et al. (2010). Weighed aliquots of Na-montmorillonite were mixed with 10 mL of Nanopure water. After mixing for 3 days, the suspensions were centrifuged, and the resulting supernatant solutions filtered with 0.2 µm filters (first 1 mL discarded). The solutions were analyzed for bromide concentrations by ICP.

3.2.1.4 Multi-component transport modeling

The diffusion data were modeled using PHREEQC v3.0 in a 1D geometry using the multi-component diffusion (MCD) capabilities of the code and in collaboration with C. Tournassat (BRGM, France). Diffusion coefficients of individual chemical species were taken from the PHREEQC.dat database. No temperature correction was done. Filter diffusion properties were explicitly taken into account as well as the dead-volume at the end of the experimental device. Filter transport parameters were derived from a previous study (Molera et al. 2003), because the same material was used in this study: θ_f = 0.25, G=2.33, height=0.082 cm. Molera and co-workers found identical G_f values for Na^+, Cs^+ and Sr^{2+} diffusion, and we considered that diffusion parameters of the filters were identical for all chemical species. Details of the system geometry are given in Figure 3.2. Constant concentrations of tracers were assigned to the upper reservoir. The renewal of the lower reservoir at each sampling time has a non-negligible effect on the diffusion gradient and thus on the recorded fluxes (Glaus et al. 2013). This effect was fully taken into account during the simulation: tracers accumulated as a function of time in the numerical cell representative of the lower reservoir; this numerical cell was reset to a zero concentration for tracers at each sampling time, and the simulation was restarted. The solution in the dead-volume was not reset to a zero concentration, thereby mimicking the “storage” effect of the solution in the tubing of the peristaltic pump. Using this calculation method, the calculated concentrations in the lower reservoir could be compared directly to the measured concentrations at each sampling time without any data pre-treatment.

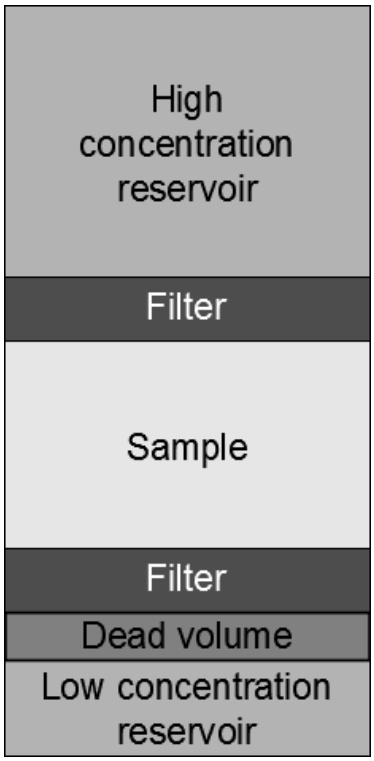

Figure 3.2. Sketch of the modeled diffusion cell system.

3.2.1.5 Molecular dynamics simulations

MD simulations of Na-Ca-Cl-Br aqueous solutions confined in a 31.5 Å wide nanopore between parallel smectite basal surfaces were carried out as in the previous research of Holmboe and Bourg (2014), in collaboration with M. Holmboe (Uppsala University, Sweden). The methodology is known to accurately predict the diffusion coefficients and activation energies of diffusion of water and sodium in smectite interlayer nanopores for pore widths ranging from 0.3 to 30 Å and temperatures ranging from 278 to 353 K (Holmboe and Bourg 2014). In brief, simulations were carried out with the program LAMMPS. Inter-atomic interactions were described with the SPC/E water model of liquid water and the CLAYFF model of mineral-water interactions. Water molecules were kept rigid using the SHAKE algorithm. Production runs were carried out in the *NVT* ensemble (constant composition, volume, and temperature) using two different initial configurations for a total duration of 105 ns (with a 1 fs time step) and were preceded by 1 ns of equilibration in the *NPT* ensemble (at P = 1 bar) and 5 ns of equilibration in the *NVT* ensemble. Electrostatic and dispersion interactions beyond 12 Å were computed with the particle-particle particle-mesh (PPPM) solver. Two-dimensional diffusion coefficients (D_{pore}) in the *xy* plane of the interlayer nanopores were calculated with the well-known Einstein relation:

$$D_{\text{pore}} = \frac{1}{2n} \lim_{\tau \to \infty} \frac{d\langle l^2 \rangle}{d\tau} \tag{3.1}$$

where n = 2 for diffusion in the *xy* plane, and $\langle l^2 \rangle$ is the mean-square displacement of the species of interest as a function of time τ. The infinite-time limit in the Einstein relation was evaluated using the slope $\langle l^2 \rangle$ versus τ for τ = 150 to 250 ps, as calculations using shorter probe time scales may not accurately reflect the infinite-time diffusive limit (Bourg and Sposito 2011).

In order to calculate D as a function of distance from the surface, the pore was divided into 0.2 Å thick slices parallel to the clay surfaces. To circumvent the effect of the finite residence time within each slice, normally being only a fraction of τ, the mean square displacement within each slice was analyzed with

Equation.(3.1) using a mended single particle trajectory. This mended single particle trajectory was constructed from all segments of trajectory data belonging to each slice by (1) appending all particles trajectories into a single particle trajectory and (2) iteratively removing the last record of any preceding trajectory segment, and then translating the succeeding segment of trajectory data so that its first trajectory record replaced the removed record in the preceding trajectory segment.

The simulated system contained 180 clay unit cells of average unit cell formula $Si_8(Al_{3.33}Mg_{0.67})O_{20}(OH)_4$, 9000 water molecules, 116 Na^+ ions, 4 Ca^{2+} ions, 3 Cl^- ions, and 1 Br^- ion (total of 34324 atoms) in a 93.305 × 90.030 × 40.913 Å simulation cell. The system was designed to approximate the conditions of a macroscopic diffusion experiment. The average unit cell formula used in our simulations was close to that of the clay used in the experiment. The solid-liquid ratio, M = 0.81 kg dm^{-3}, calculated using a smectite particle thickness of 9.4 Å (Bourg and Sposito, 2011)] was close to that used in the experiments. The average composition of the nanopore water (0.712 M Na^+, 0.247 M Ca^{2+}, 0.019 M Cl^-, 0.006 M Br^-) was selected to be roughly similar to that of the nanopore water in the diffusion experiment.

3.3 Results

3.3.1 Measurements of adsorption and diffusion at the macroscopic scale

Figure 3.3 illustrates the characteristics of the data collected. The low-concentration reservoir solution was changed very frequently during the experiment to assure that the concentration gradients between the high- and low-concentration reservoirs were nearly constant throughout the experiment. However, it was not possible to change the low-concentration reservoir solution on an even schedule, and thus, the concentrations of diffused solutes varied significantly from sample to sample, with higher concentrations observed when the elapsed time between solution changes was greater (Fig. 3.3).

One can observe from these data that the relative Br concentration (sampled concentration divided by the high concentration reservoir) was increasing faster than that for tritium, suggesting that the anion diffused faster because of charge repulsion or a lower accessible porosity than that available for tritium. Relative Ca concentrations increased much more slowly, taking weeks before significant breakthrough into the low-concentration reservoir solution (Fig. 3.3), illustrating that Ca breakthrough was likely retarded by sorption or ion exchange processes.

3.3.2 Anion accessible porosity

The static experiments yielded a total porosity of θ=0.74 based on the water-content value and a bromide concentration of 6.3×10^{-5} mol kg_{water}^{-1} when normalized to the total porosity. The external bromide concentration was 8.5×10^{-4} mol kg_{water}^{-1}. A bromide accessible porosity θ_{Br}=0.55 can be inferred from these measurements, corresponding to 74% of the total porosity.

3.3.3 Reactive transport modeling of adsorption and diffusion in the clay

3.3.3.1 Porosity and mean pore size determination

The clay was compacted at a dry density value of ρ_{dry} = 0.79 kg dm^{-3}, based on the mass of clay packed and the volume of the cell. The crystal density of clay layers (or grain or specific density, ρ_g) is about 2.84 kg dm^{-3}. Neglecting the impurities (mostly fine grained quartz), the total porosity, of the material is given by:

$$\theta = 1 - \frac{\rho_{dry}}{\rho_g} \qquad (3.2)$$

which yields a value of 0.72. This value is in excellent agreement with the value determined by water loss upon drying at 150°C (θ=0.74) after the experiment. Accordingly, the total porosity of the material was set to 0.72 for modeling purposes.

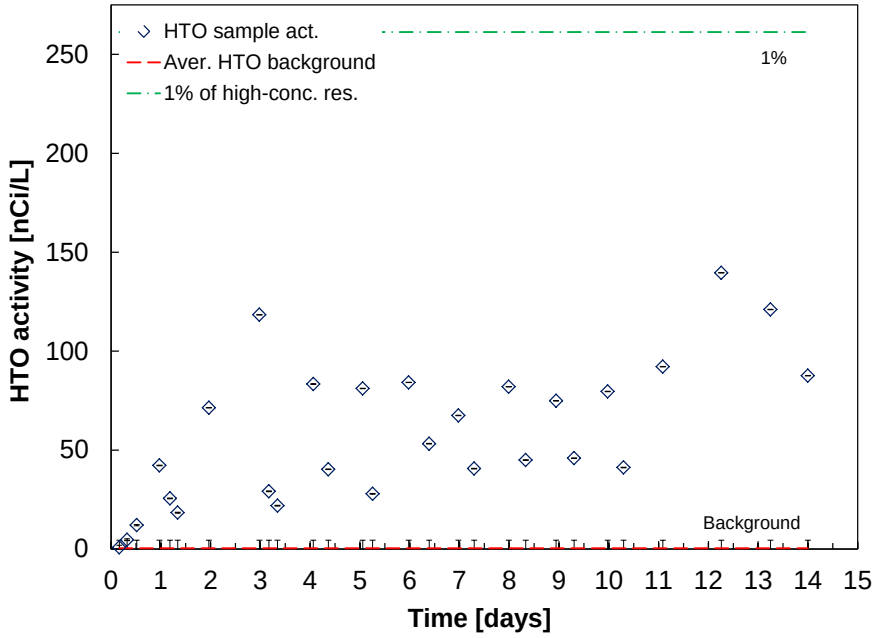
HTO sample act.
Aver. HTO background
1% of high-conc. res.
1%
Background
HTO activity [nCi/L]
Time [days]
0
50
100
150
200
250
0 1 2 3 4 5 6 7 8 9 10 11 12 13 14 15

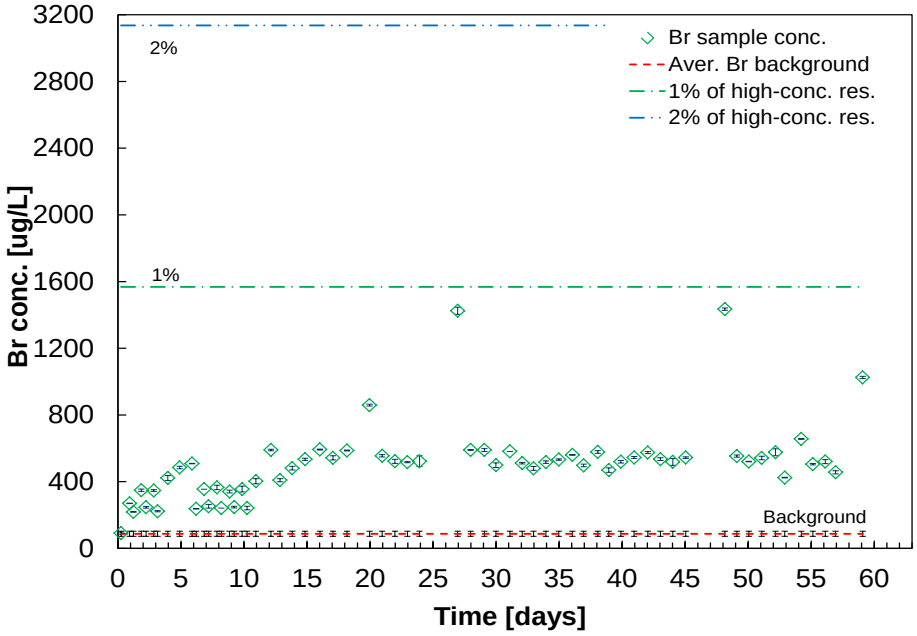
Br sample conc.
Aver. Br background
1% of high-conc. res.
2% of high-conc. res.
2%
1%
Background
Br conc. [ug/L]
Time [days]
0
400
800
1200
1600
2000
2400
2800
3200
0 5 10 15 20 25 30 35 40 45 50 55 60

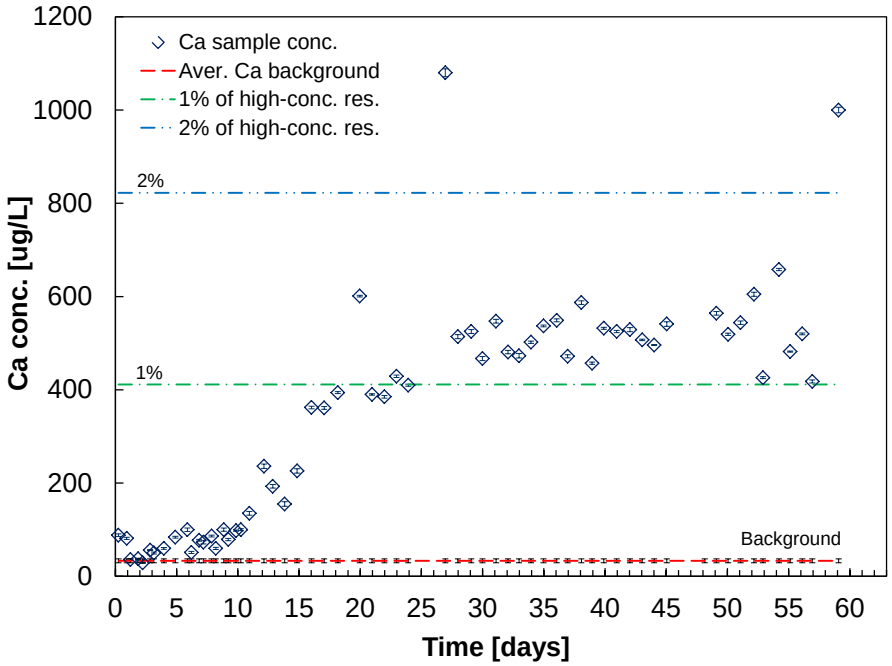

Figure 3.3. Concentrations of tritiated water (top), bromide (middle) and calcium (bottom) in samples from the low-concentration reservoir. Concentrations varied significantly due to the time lapse between changes of the low concentration reservoir solution. Dashed green curve shows the concentration that is 1% of the high concentration reservoir.

The total specific area of montmorillonite layers is *SSA*=770 m^2 g^{-1}. The cation exchange capacity of Swy-2 montmorillonite is circa 0.85-0.9 mol kg^{-1} and it follows that the surface charge is circa. σ_0 = -0.11 Coulomb-m^{-2}.

By considering that the layers have a perfect parallel and homogeneous spatial arrangement, an average pore thickness, d_{pore}^{hom}, can be estimated from:

$$d_{pore}^{hom} = \frac{\theta}{SSA/2 \times \rho_{dry} \times 10^6} \quad (3.3)$$

which yields the value 23.7 Å.

3.3.3.2 Modeling approach

The modeling strategy used here is similar to the one developed in Appelo et al. (2010). In the first step, a HTO, Br, and Ca diffusion experiment were modeled, with independent model parameters in order to derive species dependent accessible porosity/rock capacity values with related pore-diffusion coefficients. In a second step, different models were built according to various conceptual models available in the literature in order to be able to simulate the whole set of data within a single conceptual approach.

3.3.3.3 Modeling step 1.

HTO. For tritiated water (HTO), the rock capacity factor equals the total porosity (no specific retention is considered). Figure 3.4 shows that it is possible to fit HTO diffusion data by considering the total porosity value determined from sample bulk dry density (0.72) and adjusting only the geometrical factor, *G*, for the clay material (1/G = 0.047). However, it should be noted that an equally good fit could be obtained with lower or higher porosity values and corresponding lower and higher values for G (not shown). This observation demonstrates the lack of accuracy in determining HTO transport parameters at high porosities from diffusion curves only. The good agreement between the experimental measurement of water

porosity content (0.74) and the calculation from sample bulk dry density (0.72) constrains this problem. In the following, we will consider a total porosity value of $\theta = 0.72$ and a $1/G$ value of 0.047. With these parameters, D_p(water)= 1.0×10^{-10} m^2 s^{-1} and D_e(water)=7.3×10^{-11} m^2 s^{-1}. (see Appelo et al. 2010 for the relationships that determine these parameters).

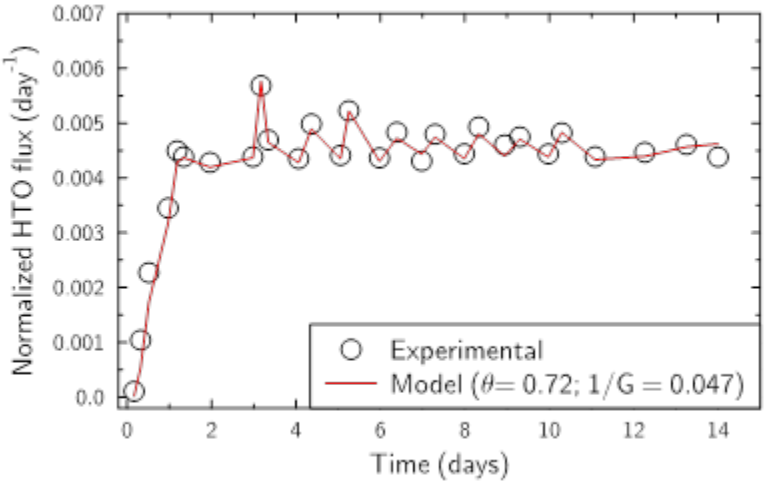

Figure 3.4. Comparison of experimental and modeled tritium flux into the low-concentration reservoir solution at a set porosity value of 0.72 and a fit value of $1/G$.

Bromide. For Br, the rock capacity factor equals the *Br^--accessible* porosity (no retention). Given the very low compaction of the material, the geometrical factor for anions should not be much different from that for the water tracer. Consequently, in a first modeling attempt, we used $G_{Br} = G_{water}$= 1/0.047. Figure 3.5 shows that experimental results are well reproduced if the porosity value is reduced to 0.46 as compared to 0.72 for water, i.e., the *Br^--accessible* porosity is 64% of the total porosity. This result is in good agreement with the experimentally measured Br- accessible porosity (described above) of 74% of the total porosity. Figure 3.5 shows that a porosity of 0.53 instead of 0.46 only decreases the $1/G_{Br}$ value to 0.041, and the available diffusion data are not sufficiently accurate to decide which is the better set of parameters. Only a comparison with independently obtained data will make it possible to refine the model. The $1/G_{Br}$ value (0.041) is lower than the $1/G_{HTO}$ (0.047), in agreement with the usually observed higher tortuosity in clay material for anions than for neutral species (Glaus et al. 2010).

Calcium. Because *Ca^{2+}-accessible* porosity is expected to be essentially the same as that of water, we expect also that the Ca^{2+} geometrical factor should not be much different from that of water. However, for Ca^{2+}, the rock capacity factor is different from the accessible porosity due to Ca^{2+} adsorption to the clay surfaces. If we consider that Ca^{2+} can diffuse with a pore diffusion coefficient, D_p(Ca), whether it is adsorbed or not, the diffusion equation simplifies to:

$$\Phi \frac{\partial c}{\partial t} = \frac{\partial}{\partial x}\left(\frac{\Phi D_p(Ca)}{G}\frac{\partial c}{\partial x}\right) \qquad (3.4)$$

where Φ is a nonphysical, effective porosity (usually Φ>1 for adsorbing species). It is possible to reproduce steady-state Ca diffusion data with $1/G$ = 0.047 and with a nonphysical effective porosity Φ equal to 11 (Figure 3.6), but this model overestimates the Ca flux in the early, transient period, thereby showing that retardation mechanisms must take place. Only the effective diffusion coefficient at steady state can be estimated: D_e(Ca)=4.1×10^{-10} m^2 s^{-1}.

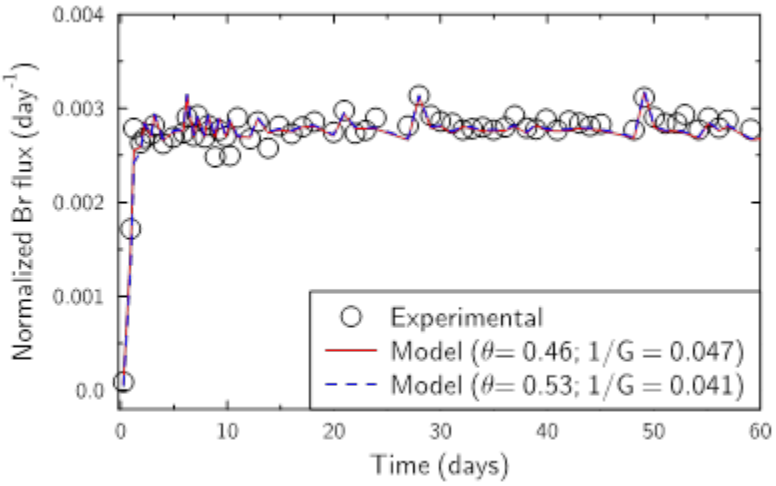

Figure 3.5. Comparison of experimental and modeled bromide ion flux into the low-concentration reservoir solution at set values of 1/*G* and fit porosity values.

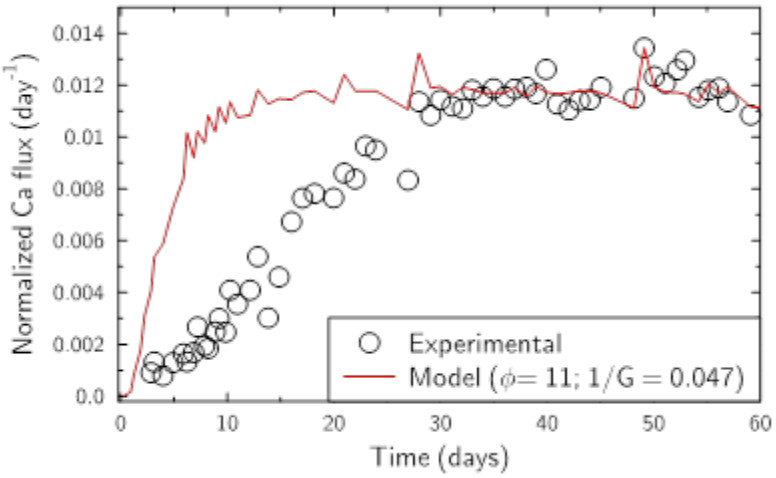

Figure 3.6. Comparison of experimental and modeled calcium ion flux into the low-concentration reservoir solution at set values of 1/*G* and fit rock capacity values.

3.3.3.4 Modeling step 2.

3.3.3.4.1 Classical pore model.

We first consider a model in which Ca and Br diffuse in the same accessible porosity, and where Ca adsorbs on the clay through a cation exchange mechanism that is responsible for its higher observed rock capacity factor. The porosity was set to 0.53 in agreement with Br accessible porosity, and two different geometric factors were considered for Br and Ca. Ca could undergo cation exchange with Na, all exchanged species being considered as immobile. For Br, $1/G_{Br}$=0.041 and this simulation is strictly equivalent to the one shown in Figure 3.6. It is also possible to fit the Ca experimental data by adjusting the $1/G_{Ca}$ value to a value of 0.47 together with a Na-Ca exchange selectivity coefficient of log $K_{Na\text{-}Ca}$ = 0.5 (using the Gaines and Thomas convention that is implemented in PHREEQC) (Figure 3.7), i.e., a value in close agreement with the values usually reported for this exchange reaction (Bourg and Sposito,

2011). As $1/G_{Ca}$ is an order of magnitude higher than $1/G_{Br}$ and $1/G_{HTO}$, it means that Ca diffusion is enhanced by a factor of ten as compared to HTO or Br diffusion, while having access to a similar porosity.

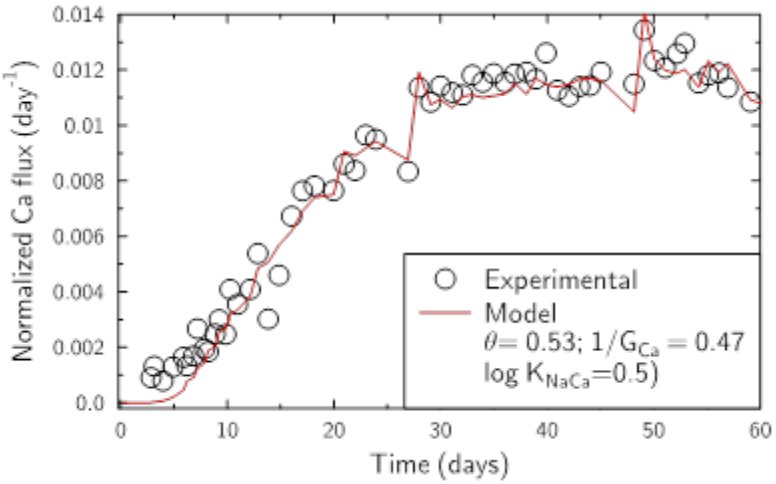

Figure 3.7. Comparison of experimental and modeled calcium ion flux into the low-concentration reservoir solution at a set value of $1/G$, ion exchange, and fit porosity value.

3.3.3.4.2 Single porosity with diffuse layer model

In this model, the clay-layer surface charge is compensated by the condensation of cations and the exclusion of anions in a diffuse layer. Diffusion of water and ions is attributed to the additive contributions of the "free" water, where electro-neutrality prevails, and of the diffuse layer water, where cation concentration is higher than anion concentration (Appelo et al. 2010). The diffuse layer average composition is not obtained by solving the Poisson-Boltzmann equation, but by using a so-called "Donnan" equilibrium model, i.e., a mean potential model, assuming a mean water density of 1 kg dm^{-3} in the diffuse layer. The distribution of water among the "free" water and the diffuse layer water can be calculated according to the method from Appelo et al. (2010) as explained below.

If we consider that a fraction, f, of the porosity is "free" water and a fraction 1-f to be located in the diffuse layer, it follows that:

$$\theta_{Br} \times C_{Br,free} = f\theta_{HTO} \times C_{Br,free} + (1-f)\theta_{HTO} C_{Br,EDL} \quad (3.5)$$

where $C_{Br,free}$ and $C_{Br,EDL}$ are the bromide concentration in the free water and in the diffuse layer respectively. The mean concentration in the diffuse layer is related to the concentration in the free water through:

$$C_{Br,EDL} = C_{Br,free} \exp\left(\frac{F\psi_D}{RT}\right) \quad (3.6)$$

And it follows:

$$\frac{F\psi_D}{RT} = \ln\left(\frac{\frac{\theta_{Br}}{\theta_{HTO}} - f}{1-f}\right) \quad (3.7)$$

Next, we define σ_D as the surface charge that is compensated in the diffuse layer and that is thus related to the charge balance in the diffuse layer:

$$(1-f)\theta_{HTO}\sum_i z_i C_{i,EDL} = -1000 \times SSA \times \frac{\sigma_D}{F} \times \rho_{dry} \tag{3.8}$$

For the conditions of Br diffusion (and for the case where no Ca has diffused yet, *i.e.* only Na compensates the surface charge):

$$\begin{aligned}&(1-f)\theta_{HTO}\left(C_{Na,Bulk}\exp\left(\frac{-F\psi_D}{RT}\right) - C_{Na,Bulk}\exp\left(\frac{F\psi_D}{RT}\right)\right)\\ &= -1000 \times SSA \times \frac{\sigma_D}{F} \times \rho_{dry}\end{aligned} \tag{3.9}$$

Rearranging,

$$\sigma_D = \frac{-2F\theta_{HTO}C_{Na,Bulk}(1-f)\sinh\left(-\ln\left(\dfrac{\frac{\theta_{Br}}{\theta_{HTO}}-f}{1-f}\right)\right)}{1000 \times SSA \times \rho_{dry}} \tag{3.10}$$

Figure 3.8 shows that for our experimental conditions, if the total surface charge is compensated in the diffuse layer, it follows that the f value is about the same as the $\frac{\theta_{Br}}{\theta_{HTO}}$ value (~0.74), meaning that Br is almost entirely confined in the free water volume. On the other hand, if all the porosity volume is considered to be occupied by the diffuse layer (i.e., f = 0), then the effective surface charge must be less than 10% of the total surface charge, meaning that more than 90% of the charge must be screened by surface-complexing cations.

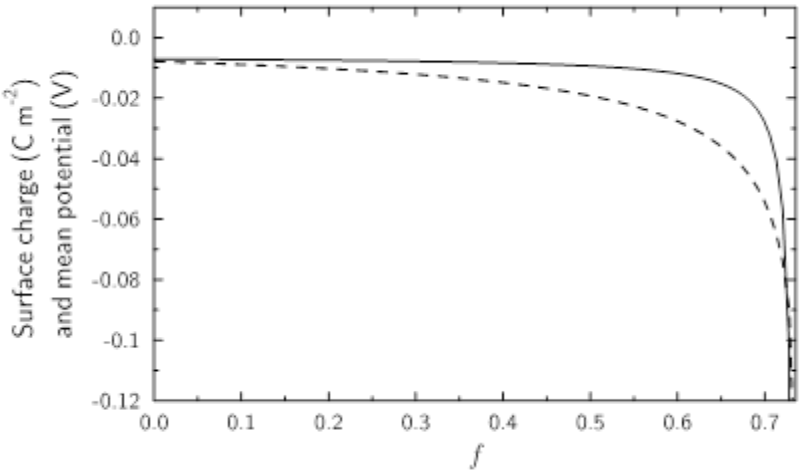

Figure 3.8. Relationship between the diffuse layer mean potential, surface charge compensated in the diffuse layer, and ratio of free water in the porosity, via Equations. (3.7)-(3.10).

Next, we consider for a first simulation run that: (i) the diffuse layer has the same diffusion properties as bulk water, and (ii) no surface charge compensation occurs other than the compensation in the diffuse layer. The geometrical factor of Ca is set equal to that of HTO. Figure 3.9 shows that the calculated Ca flux is too high in comparison to the experimental data. Moreover, the Ca retardation is not sufficient.

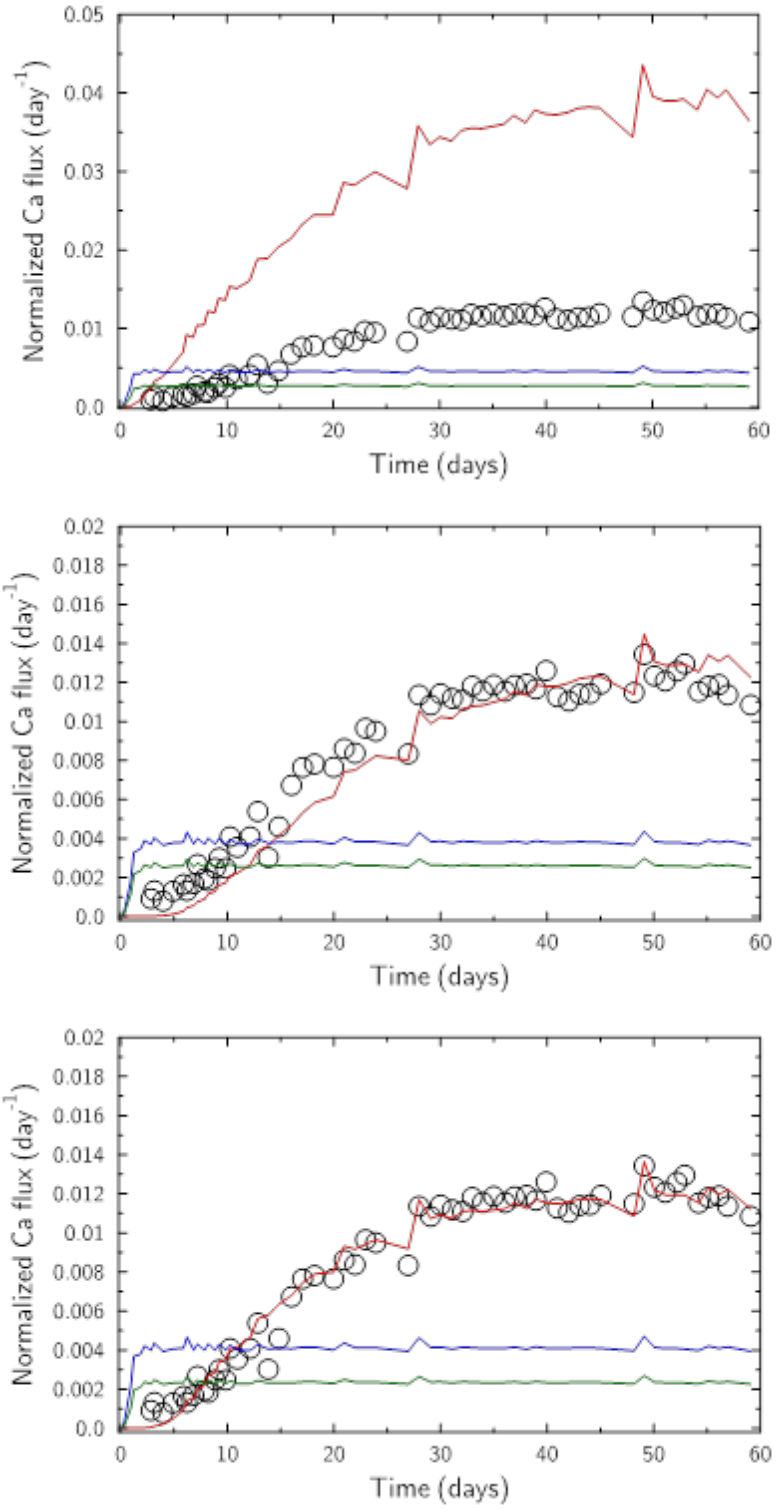

Figure 3.9. Single porosity model with diffuse layer and surface complexation. Top: no surface complexation, diffusion properties of the diffuse layer are the same as the diffusion properties of the bulk water. Middle: surface complexation according to model 1 (log KNa = -0.7). Bottom: surface complexation model according to model 2 (log KNa = 0.8).

These two deficiencies in the model can be solved: (i) by considering that the diffusivity in the diffuse layer is less than in bulk water, and/or (ii) by considering Ca (and Na) surface complexation. Na and Ca surface complexation were taken into account by considering the following reactions in the framework of a double layer surface complexation model (Parkhurst and Appelo, 1999):

$$Surf^- + Na^+ \rightleftharpoons SurfNa \quad \log K_{Na} \tag{3.11}$$

$$2\ Surf^- + Ca^{2+} \rightleftharpoons Surf_2Ca \quad \log K_{Ca} \tag{3.12}$$

As explained in Appelo et al. (2010), $\log K_{Ca}$ is constrained by the relative affinities of Ca and Na for the surface with $\log K_{Ca} - 2 \log K_{Na} \sim 0.5\text{-}1$. Varying the $\log K_{Na}$ value enables one to vary the extent of surface charge compensation by surface complexes. A large range of K_{Na} values can be found in the literature, depending on the model used and the representation of the interface between the clay surface and the solution. With a $\log K_{Na} = -0.7$ (Appelo et al. 2010, EDL model 1), 74% of the surface charge is compensated by the diffuse layer, thus corresponding to a "free" pore water volume of 70% of the total porosity (Figure 3.9, middle). With a $\log K_{Na} = 0.8$, 30% of the surface charge is compensated by the diffuse layer, thus corresponding to a "free" pore-water volume of 60% of the total porosity (Figure 3.9, bottom). Hence, for our system, the choice of $\log K_{Na}$ within a reasonable range of values has little influence on the volume repartition between the diffuse layer and the "free" water.

Ca diffusion data can be reproduced using either EDL models 1 ($\log K_{Na} = -0.7$) or 2 ($\log K_{Na} = 0.8$) by adjusting the $\log K_{Ca}$ value together with the diffusivity in the diffuse layer, thereby showing the cross-correlation of the three parameters and reminding us that available macroscopic-scale data do not strongly constrain current theories of the clay properties (Figure 3.9).

3.3.4 Molecular Dynamics Simulations of Smectite Nanopores

As mentioned in the Methods section above, the simulated system contained 180 clay unit cells of average unit cell formula $Si_8(Al_{3.33}Mg_{0.67})O_{20}(OH)_4$, 9000 water molecules, 116 Na^+ ions, 4 Ca^{2+} ions, 3 Cl^- ions, and 1 Br^- ion (total of 34,324 atoms) in a $93.305 \times 90.030 \times 40.913$ Å simulation cell. Molecular dynamics simulations of the average density of ions and water as a function of distance from the clay surface are shown in Figure 3.10. Simulation results are broadly consistent with our previous study of Na-Ca-Cl solutions of higher salinity (0.3 to 1.8 $mol_c\ dm^{-3}$) in 6 nm wide clay interlayer nanopores (Bourg and Sposito, 2011), despite significant methodological differences (our previous simulations used higher concentrations and a larger pore size, as noted above, as well as a different MD simulation code, different inter-atomic potential parameters for Na^+ and Cl^-, and a rigid clay framework). The simulation predicts the existence of three ordered water layers at $z = 6.1$, 9.5, and 12.4 Å. If the peak locations are expressed relative to the plane of surface O atoms (with a rescaled coordinate $z^* = z - 3.22$ Å), the water density peaks are located at $z^* = 2.9$, 6.3, and 9.2 Å. The spacing between the water density peaks is close to the diameter of a water molecule, showing that the water layering arises from the steric packing of water molecules on the clay surface.

Ion density profiles show that Na^+ and Ca^{2+} are attracted to, and Cl^- and Br^- are repulsed from, the vicinity of the clay surface, as expected from the negative structural charge of the clay lamellae. For all four ionic species, the density profiles show two peaks near the clay surface: a first peak at $z = 7.65 \pm 0.1$ Å (for all four ions) and a second peak at $z = 9.95 \pm 0.1$ Å (for cations) or 10.35 ± 0.1 Å (for anions). In the context of the well known triple-layer model (TLM), the two peaks of the cation density profiles indicate adsorption as outer-sphere surface complexes (OSSC) and in the diffuse ion swarm (DIS). The OSSC density peaks accounts for 35% of Na^+ ions and 65% of Ca^{2+} ions in our system. The existence of two peaks in the anion density profiles are inconsistent with mean-field theories of ion adsorption on charged surfaces, such as the TLM, which suggests that these features arise from ion-ion or ion-water correlations that are not taken into account by these theories. The coincidence of the cation and anion density peaks suggest that the position of the peaks is strongly influenced by water density layering at the clay-water interface, even though the position of the peaks is not perfectly registered with the water-density features

(the first ion density peak is located close to the minimum between the first and second water layers, whereas the second ion density peak almost coincides with the second water layer).

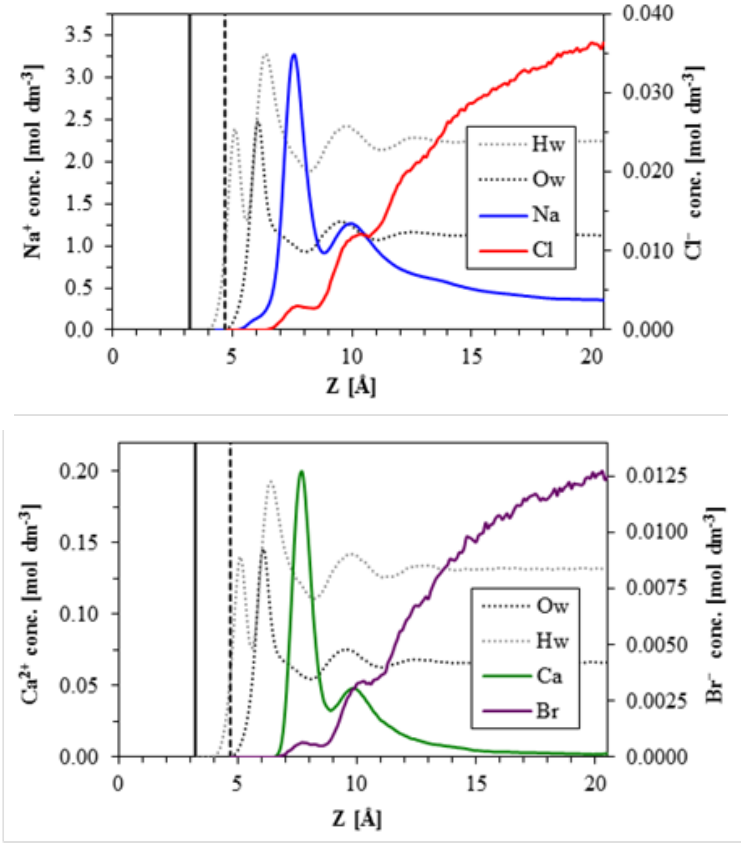

Figure 3.10. MD simulation of the average density profiles of water and ions as a function of distance in the direction normal to the clay surface, from the mid-plane of the clay sheet (z = 0 Å) to the mid-plane of a nanopore (z = 20.45 Å). Vertical lines show the location of the plane of surface O atoms (solid line, z = 3.23 Å) and the location of the Gibbs dividing surface (dashed line, z = 4.7 Å). The solid curves show the density profiles of Na^+ and Cl^- (upper figure) and Ca^{2+} and Br^- (lower figure) using a different vertical scale for each ion. The dotted black and gray lines show the density profiles of water O and H atoms with an arbitrary vertical scale.

Values of the average ion concentration in the mid-plane of the nanopore, reported in Table 3.1, show that water in the mid-plane contains significantly more moles of cationic charge (q_+ = 0.3659 mol_c dm^{-3}) than moles of anionic charge (q_- = 0.0484 mol_c dm^{-3}). This indicates that the EDLs formed on the two clay surfaces overlap in the center of the nanopore, a phenomenon that is known to strongly influence the swelling properties and semi-permeable membrane properties of compacted clays. To a first approximation, we can apply a Donnan equilibrium model to estimate the composition of a hypothetical bulk-liquid-like component that would be in equilibrium with the water in the mid-plane of our interlayer nanopore, by applying a charge-balance relation to ion concentrations, $C_{i,\mathrm{bulk}}$, in the hypothetical bulk solution:

$$\sum_i z_i C_{i,\mathrm{bulk}} = 0 \qquad (3.13)$$

where z_i is the valence of the ion i of interest, and a Boltzmann relation between concentrations at the interlayer mid-plane ($C_{i,\text{mid-plane}}$) and in the bulk solution:

$$C_{i,\text{mid-plane}} = C_{i,\text{bulk}} e^{\frac{-z_i F \psi_{\text{mid-plane}}}{RT}} \tag{3.14}$$

where $\psi_{\text{mid-plane}}$ is the electrostatic potential at the interlayer mid-plane (relative to a value of zero in the hypothetical bulk solution), F is Faraday's constant, R is the ideal gas constant, and T is absolute temperature. Application of Equations (3.13)-(3.14) to the values of $C_{i,\text{mid-plane}}$ in Table 3.1 yields $\psi_{\text{mid-plane}}$ = -25.9 mV and the values of $C_{i,\text{bulk}}$ shown in the last row in Table 3.1.

Alternatively, the full Poisson-Boltzmann (PB) equation can be solved numerically and the "free" water chemical composition can be adjusted to match the MD concentration profiles. A distance of closest approach corresponding to the position of first adsorption peak maximum was chosen: the effective pore size was thus reduced to 25.8 Å. The surface charge was set to -0.114 C m^{-2}. Na, Ca, Cl, and Br concentrations in "free" water were varied to match the MD concentration profiles. Actually, only Na and Ca concentrations were fitted due to (i) the electroneutrality condition in free water and (ii) the relationship $C_{Cl}=3\times C_{Br}$. From the concentration profiles, it is possible to calculate a mean concentration in the pore. The excellent agreement for anion profiles between MD calculations and PB prediction justifies the use of the PB equation to estimate the anion accessible porosity in pores of similar size and for similar ionic strength and solution composition (Figure 3.11).

The values of $C_{i,\text{pore}}$ and $C_{i,\text{free}}$ in Table 3.1 allow us to quantify several ion adsorption (or negative adsorption) coefficients at the nanopore scale. The amount of adsorbed solute per mass of clay q_i can be calculated according to the relation:

$$q_i = \frac{C_{i,\text{pore}} - C_{i,\text{pore}}}{M} \tag{3.15}$$

MD simulation predictions of the diffusion coefficients of water and ions in bulk liquid water (D_{bulk}) and in the clay interlayer nanopore (D_{pore}), shown in Table 3.2, indicate that all species diffuse more slowly in the nanopores than in bulk liquid water. The influence of confinement, quantified by the nanopore confinement effect $q_{\text{nano}} = D_{\text{pore}}/D_{\text{bulk}}$, is identical for all species except Ca^{2+} (Table 3.2). This effect is thought to arise from the fact that calcium is strongly concentrated near the clay surface, where water and solutes tend to diffuse more slowly. Predictions of the self-diffusion coefficient of water O atoms as a function of distance from the surface (Figure 3.12) indicate that in the region between the first and second water layers (where a large fraction of the cations is adsorbed as OSSC), water diffuses roughly 80% as fast as bulk liquid water.

Table 3.1. Molecular dynamics simulation predictions of the average ion concentration in the entire pore ($C_{i,\text{pore}}$), in the mid-plane of the pore ($C_{i,\text{mid-plane}}$), and in a hypothetical bulk solution in Donnan equilibrium with the mid-plane of the pore ($C_{i,\text{bulk}}$).

	Br	Cl	Ca	Na
	MD			
C_{pore} (mol dm^{-3})	$6.17\text{x}10^{-3}$	$1.85\text{x}10^{-2}$	$2.47\text{x}10^{-2}$	$7.16\text{x}10^{-1}$
$C_{\text{mid-plane}}$ (mol dm^{-3})	$1.25\text{x}10^{-2}$	$3.59\text{x}10^{-2}$	$2.40\text{x}10^{-3}$	$3.61\text{x}10^{-1}$
	Donnan			
C_{bulk} (mol dm^{-3})	$3.42\text{x}10^{-2}$	$9.83\text{x}10^{-2}$	$3.2\text{x}10^{-4}$	$1.32\text{x}10^{-1}$
	Poisson-Boltzmann			
C_{bulk} (mol dm^{-3})	$3.42\text{x}10^{-2}$	$1.03\text{x}10^{-1}$	$3.5\text{x}10^{-4}$	$1.36\text{x}10^{-1}$
C_{pore} (mol dm^{-3})*	$5.7\text{x}10^{-3}$	$1.7\text{x}10^{-2}$	$1.9\text{x}10^{-2}$	$6.52\text{x}10^{-1}$
q (mol kg^{-1})	$-3.46\text{x}10^{-2}$	$-9.83\text{x}10^{-2}$	$3.0\text{x}10^{-2}$	$7.19\text{x}10^{-1}$
ϕ_a/ϕ (-)	0.180	0.188	n.a.	n.a.
K_d (dm^3 kg^{-1})	n.a.	n.a.	93.8	5.45

* normalized to the total pore size (x25.8/35.54)

Table 3.2. MD simulations of the average diffusion coefficients of ions and water in the clay nanopores (D_{pore}) and in bulk liquid water (D_{bulk}). Values of D_{bulk} are corrected for the artifact that causes a simulation cell size dependence of D in MD simulations of bulk fluids; for D_{pore} no correction is needed, as shown in our previous study (Holmboe and Bourg, 2014). The last row shows the nanopore confinement effect $q_{\text{nano}} = D_{\text{pore}}/D_{\text{bulk}}$.

	Br	Cl	Ca	Na	H_2O
D_{pore} (10^{-9} m^2 s^{-1})	1.32±0.15	1.22±0.07	0.47±0.04	0.80±0.01	2.05±0.01
D_{bulk} (10^{-9} m^2 s^{-1})	1.58±0.02	1.68±0.08	0.85±0.04	1.08±0.09	2.68±0.03
q_{nano} (-)	0.83±0.09	0.73±0.05	0.55±0.05	0.74±0.06	0.77±0.01

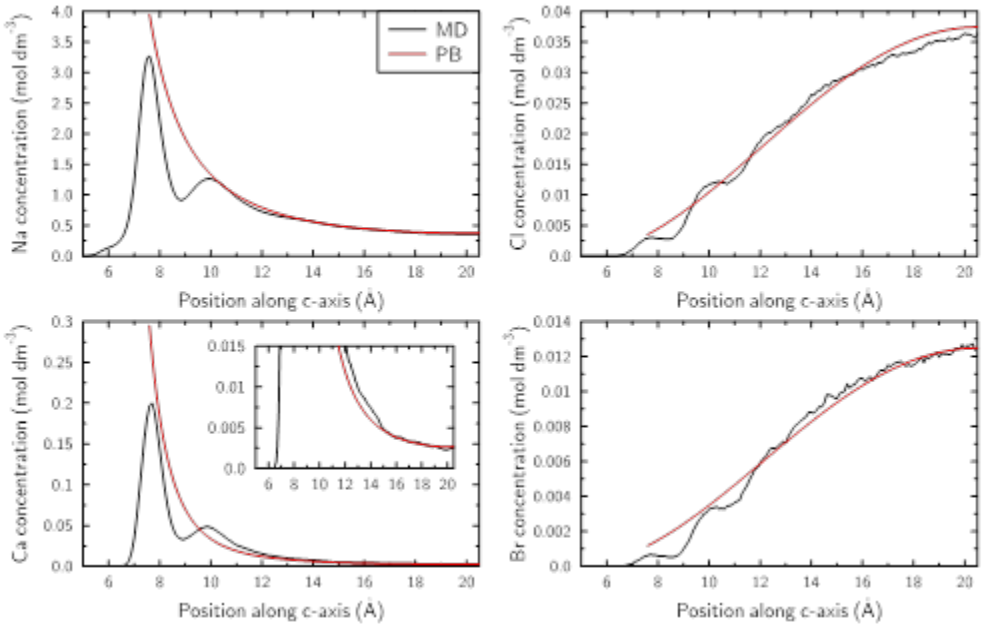

Figure 3.11. Comparison of cation and anion profiles between MD results and Poisson-Boltzmann equation resolution.

3.4 Discussion

3.4.1 Is free water present in compacted montmorillonite?

The present experiment deals with a loosely compacted montmorillonite. However, the mean pore size (~23.7 Å) is on the order of eight water layers. In similar conditions, the resolution of the Poisson-Boltzmann equation and the MD results agreed, and the solution in the center of the pore was found to be charge unbalanced, with more cationic charges than anionic charges. Note that these calculations were representative of slightly larger pore and ionic strength than those of the diffusion experiment, meaning that the charge unbalance was even underestimated as compared to the value that could be calculated with actual experimental conditions. From those considerations, it should then be concluded that no free water was present in the porosity of the clay sample, and that a single porosity model with the diffuse layer occupying all the space might be appropriate, as for example the model proposed by Birgersson and Karnland (2009). However, this kind of model leads to an overestimation of the actually measured anion exclusion as exemplified by Figure 8. MD results support this conclusion by showing too much anion exclusion, as compared to the measurement in conditions that are otherwise less favorable to anion exclusion than the experimental one. Finally, the excellent agreement of MD results with the resolution of the Poisson-Boltzmann equation justifies the use of the PB model to estimate anion exclusion accurately (Figure 3.11). However, such a calculation yields too much anion exclusion.

Consequently, homogeneous pore models where only a diffuse layer is present cannot be successful at describing correctly the mass balance between surface charge, anions, and cations in the porosity, and it is necessary to consider that free water is present in the porosity.

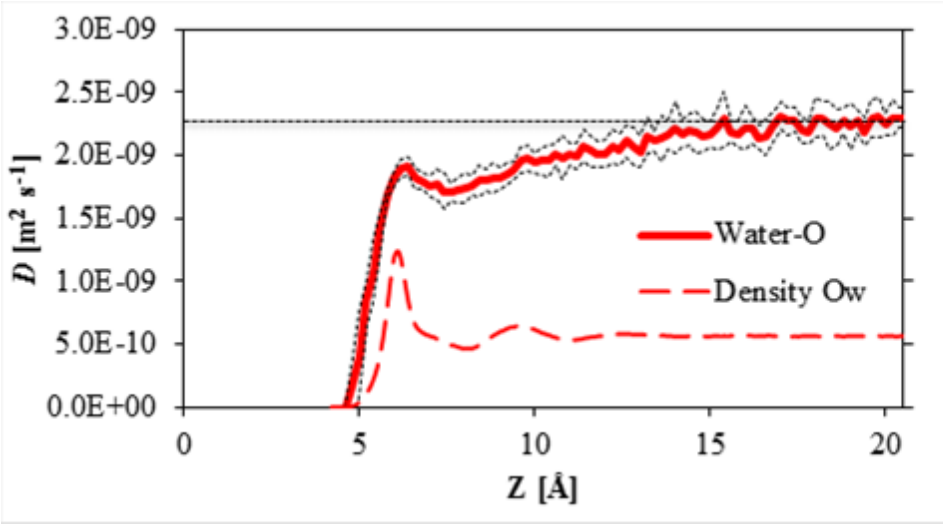

Figure 3.12. Molecular dynamics simulation of the average diffusion coefficient of water O atoms in the *xy*-plane as a function of distance from the clay surface (solid line, with confidence intervals shown as dashed lines). The density profile of water O atoms is shown by the thick dashed line. The self-diffusion coefficient of bulk liquid water is shown by the horizontal dashed line.

3.4.2 Is an average pore model with free water and diffuse layer/surface complexation physically relevant?

The model result depicted in Figure 3.7 is representative of a single pore model with surface complexation, where all the surface charge is compensated by adsorbed cations, leaving no charge to be compensated in a diffuse layer. Br and Ca diffusion data are fitted adequately using this model, but it is not possible to fit HTO data (not shown) satisfactorily, because the considered porosity corresponds to the anion accessible porosity and not the total porosity. This problem could be circumvented by considering the adsorption of the water molecule corresponding to the hydration shells of adsorbed Na and Ca (not shown). The Ca diffusivity in the bulk water must be increased by a factor of ten, as compared to the diffusivity of Br, in order to fit the data. It is difficult to justify the physical meaning of such an increase of the Ca diffusion coefficient, unless it is considered that this increase compensates the assumed zero mobility of surface complexed Ca. Indeed, the MD results indicate that outer-sphere surface complexes of Na and Ca have a non-negligible mobility parallel to the surface. This single pore model can thus be successful at describing the system as a whole, if the adsorption of water molecules is considered and if the mobility of adsorbed ions/molecules is taken into account. However, it remains in poor agreement with the MD results that predict the presence of a diffuse layer in accordance with the Poisson-Boltzmann model prediction.

If the presence of a diffuse layer is considered in a single porosity model, then it must agree quantitatively with the relationship that governs the distribution of water between free and diffuse layer water. Figure 3.9 shows clearly that this model implies the necessary assumptions of: (1) the presence of non- (or negligibly) mobile surface complexes to explain the Ca retardation, and (2) a lower diffusivity of Ca in the diffuse layer than in the bulk water. These two features are supported by the MD results. The diffusion data alone do not enable one to quantify with precision the surface complexation model parameters (especially log K_{Na}). In addition, the necessary decrease in Ca mobility in the diffuse layer is not in quantitative agreement with the decrease in the Ca diffusion coefficient that is calculated with the MD trajectories. Finally, it is possible to estimate a mean diffuse layer thickness with:

$$d_D = \frac{\theta_{EDL}}{SSA \times \rho_{dry} \times 10^6} \quad (3.16)$$

The resulting value is d_D = 3.6 Å. This value is clearly nonphysical: it represents only one water molecule diameter. As a conclusion, this last single pore model fails at giving a physically consistent picture of the processes at work.

Obviously, the single porosity model is an oversimplification of a complex system, and the corresponding derived parameters consistent with that model result from the integration of several processes, thus explaining why so many different models are available to describe very similar data in the literature. The model differences depend strongly on the authors' choices for the processes that are coupled together.

The above detailed evaluation of single pore models with regards to molecular information (on the one hand) and experimental diffusion and static data (on the other) is good evidence that the distribution of pore size (at least interlayer, mesopores, and macropores) is indeed an important feature that must be taken into account to understand water, anion, and cation diffusivity in clay materials (Tournassat and Appelo, 2011). In this work, multi-porosity models were not proposed because parameterization of such models would have been underconstrained by the available data. Detailed characterization of clay-material pore structure down to the resolution of the interlayer size would greatly help to constrain such models.

3.5 Summary

This section examines the consistency of macroscopic measurements, electrical double layer (EDL)-based models, and molecular-scale simulations of clay media. Macroscopic-scale measurements of the adsorption and diffusion of trace levels of calcium (Ca^{2+}), bromide (Br^-), and tritiated water (HTO) in a loosely compacted, water-saturated Na-montmorillonite are presented. In order to aid in the interpretation of the macroscopic-scale data, as well as to challenge the fundamental assumptions inferred by different pore/transport models commonly used in the diffusion literature, molecular dynamics (MD) simulations of adsorption and diffusion in individual clay interlayer nanopores are presented at similar solid-liquid ratio and electrolyte composition as in the laboratory diffusion experiments.

The results from the macroscopic-scale adsorption and diffusion experiments and MD simulations of the montmorillonite diffusion experiment allow a critical test of various transport/pore models, by carefully evaluating the physical meaning of their related fitting parameters on a single set of data. Hence, by evaluating the results using a multi-component reactive transport (diffusion) approach with the different transport/pore models, we highlight the difficulty in constraining current theories of the properties of clay barriers using transport modeling alone.

The report reaches the following conclusions with regard to "average pore" models:

- Some models cannot reproduce the data: a simple Donnan model applied to the whole porosity simply does not comply with the actual measured anion accessible porosity;
- The "classical pore model" without diffuse layer consideration enables modeling of the Br and Ca diffusion data, but for Ca we need to consider a very high diffusivity as compared to water. This is not in agreement with the MD calculation and does not make sense from a physical point of view;
- Pore models with the consideration of the diffuse layer can reproduce the data well in a single run, and diffusion or surface complexation parameters appear to have physically meaningful values. But the calculated diffuse layer thickness with these models is nonsensical, and the diffusivity in the diffuse layer is far too low compared to that estimated from MD simulations.

- The detailed evaluation of single pore models presented in this report, with regard to molecular information on the one hand and experimental diffusion and static data on the other hand, demonstrates the need to consider a *distribution* of pore size as the important feature that must be taken into account to understand water, anion, and cation diffusivity in clay materials.

4. SUMMARY

(1) Modeling Coupled THMC Processes in the EBS (Chapter 2)

We are developing and applying coupled THMC models for the analysis of EBS coupled processes in bentonite-backfilled repositories. We based this development on the extension of the Barcelona Basic Model (BBM) to a dual-structure model for expansive clay, such as bentonite. The dual-structure model has been found to give results that are in better agreement with observations, in particular the rate of buffer resaturation, by representing identifiable physical mechanisms not treated by the original BBM model. Therefore, this model improvement reduces the modeling uncertainty for THM processes in a bentonite buffer. Specific accomplishments are as follows:

- We completed implementation of the dual-structure model into TOUGH-FLAC, tested the model against literature data from experiments and independent models, and have successfully modeled and reproduced observed behavior for laboratory tests on expansive clay under increasing confining stress.
- We completed simulations for a generic high-level nuclear waste repository showing the importance of considering the dual-structure behavior on the resaturation and swelling of the buffer, including a delayed resaturation as has also been experimentally observed.
- We applied the previously developed and implemented CM coupling model and TOUGHREACT-FLAC3D to simulate the effect of illitization on swelling pressure at high temperature for a generic repository.
- We upgraded the CM coupling scheme based on the dual-structure model for expansive clay and implement the new scheme into the TOUGHREACT-FLAC3D simulator.

Recommended work for FY15 includes:

- Continue to validate and improve the dual-structure model by testing it on new experimental data available through international collaborative DECOVALEX and Mont Terri projects, as well as any new data available in the literature.
- Based on modeling of long-term evolution and the outcome of model validations against experimental data, develop an experimental protocol for validation and for determining key parameters that will minimize uncertainties in the long-term model predictions.
- Testing and validation TOUGHREACT-FLAC3D with the newly developed and implemented CM model against experimental data.
- Evaluate the long-term THMC behavior of EBS bentonite through a mechanistic THMC analysis using TOUGHREACT-FLAC and the dual-structure model with new the CM coupling scheme.
- Develop CM coupling relationships to describe effects of cementation (silica precipitation) on mechanical properties of bentonite (transition from plastic to brittle).

(2) Ion Adsorption and Diffusion in Smectite Clay Barriers (Chapter 3)

This section examines the consistency of macroscopic measurements, electrical double layer (EDL)-based models, and molecular-scale simulations of clay media for adsorption and diffusion of trace levels of calcium (Ca^{2+}), bromide (Br^-), and tritiated water (HTO) in a loosely compacted, water-saturated Na-montmorillonite. Molecular dynamics (MD) simulations are also conducted and used to aid the interpretation of adsorption and diffusion processes in individual clay interlayer nanopores. The MD simulations allow a critical test of various transport/pore models by carefully evaluating the physical meaning of their related fitting parameters on a single set of data. These results highlight the difficulty in constraining current theories of the properties of clay barriers using transport modeling alone. Specific accomplishments and conclusions are as follows:

- Some models cannot reproduce the data: a simple Donnan model applied to the whole porosity simply does not comply with the actual measured anion accessible porosity;
- The "classical pore model" without diffuse layer consideration enables modeling of the Br and Ca diffusion data, but for Ca we need to consider a very high diffusivity as compared to water. This is not in agreement with the MD calculation and does not make sense from a physical point of view;
- Pore models with the consideration of the diffuse layer can reproduce the data well in a single run, and diffusion or surface complexation parameters appear to have physically meaningful values. But, the calculated diffuse layer thickness with these models is nonsensical and the diffusivity in the diffuse layer is far too low as compared to that estimated from MD simulations;
- The detailed evaluation of single pore models presented in this report, with regard to molecular information on the one hand and experimental diffusion and static data on the other hand, demonstrates the need to consider a *distribution* of pore size as the important feature that must be taken into account to understand water, anion, and cation diffusivity in clay materials.

Recommended work for FY15 includes:

- Conduct detailed characterization of clay-material pore structure down to the resolution of the interlayer size to provide sufficient data to constrain and use more complex multi-porosity models.

ACKNOWLEDGMENT

Funding for this work was provided by the Used Fuel Disposition Campaign, Office of Nuclear Energy, of the U.S. Department of Energy under Contract Number DE-AC02-05CH11231 with Lawrence Berkeley National Laboratory.

REFERENCES

Alonso, E.E., Alcoverro, J., Coste, F., Malinsky, L., Merrien-Soukatchoff, V., Kadiri, I., Nowak, T., Shao, H., Nguyen, T.S., Selvadurai, A.P.S., Armand, G., Sobolik, S.R., Itamura, M., Stone, C.M., Webb, S.W., Rejeb, A., Tijani, M., Maouche, Z., Kobayashi, A., Kurikami, H., Ito, A., Sugita, Y., Chijimatsu, M., Borgesson, L., Hernelind, J., Rutqvist, J., Tsang, C., Jussila, P. The FEBEX benchmark test: case definition and comparison of modeling approaches. Int. J. Rock Mech. Min. Sci., 42, 611–638 (2005).

Alonso, E.E., Vaunat, J., Gens, A. Modelling the mechanical behaviour of expansive clays. Engineering Geology, 54, 173–183 (1999).

Altmann, S., Tournassat, C., Goutelard, F., Parneix, J.C., Gimmi, T., Maes, N., 2012. Diffusion-driven transport in clayrock formations. Applied Geochemistry 27, 463–478.

Appelo, C.A.J., Van Loon, L.R., Wersin, P., 2010. Multicomponent diffusion of a suite of tracers (HTO, Cl, Br, I, Na, Sr, Cs) in a single sample of Opalinus Clay. Geochimica et Cosmochimica Acta 74, 1201–1219.

Birgersson, M., Karnland, O., 2009. Ion equilibrium between montmorillonite interlayer space and an external solution: Consequences for diffusional transport. Geochimica et Cosmochimica Acta 73, 1908–1923.

Bourg, I.C., Sposito, G., 2011. Ion exchange phenomena, in: Handbook Soil Science, second edition.

Corkum, A.G., Martin, C.D., 2007. The mechanical behaviour of weak mudstone (Opalinus Clay) at low stresses. Int. J. Rock Mech. Min. Sci., 44, 196–209.

Davis J., Rutqvist J., Steefel C., Tinnacher R., Vilarrasa V., Zheng L., Bourg I., Liu H.-H., and Birkholzer J. Investigation of Reactive Transport and Coupled THMC Processes in the EBS: FY13 Report. Prepared for U.S. Department of Energy, Used Fuel Disposition, FCRD-UFD-2013-000216, Lawrence Berkeley National Laboratory (2013).

Di Maio, C. Exposure of bentonite to salt solution: osmotic and mechanical effects. Géotechnique 46(4): 695-707 (1996).

Di Maio, C., Discussion on exposure of bentonite to salt solution: osmotic and mechanical effects. Geotechnique XVVIII (3), 433–436 (1998).

Gens, A, Alonso, E. A framework for the behaviour of unsaturated expansive clays. Can. Geotech. J. 29, 1013–1032 (1992).

Gens, A. Soil - environmental interactions in geotechnical engineering. Geotechnique, 60, 3–74 (2010).

Gens, A., Sánchez, M., Guimarães, L. do N., Alonso, E.E., Lloret, A., Olivella, S., Villar, M.V., Huertas, F. A full-scale in situ heating test for high-level nuclear waste disposal: observations, analysis and interpretation. Geotechnique, 59(4), 377–399 (2009).

Gens, A., Sánchez, M., Sheng, D. On constitutive modelling of unsaturated soils. Acta Geotechnica, 1, 137–147 (2006).

Gens, A., Vaunat, J., Garitte, B., Wileveau, Y. In situ behaviour of a stiff layered clay subject to thermal loading, observations and interpretation. Geotechnique, 57(2), 207–228 (2007).

Glaus, M.A., Frick, S., Rosse, R., Van Loon, L.R., 2010. Comparative study of tracer diffusion of HTO, Na-22(+) and Cl-36(-) in compacted kaolinite, illite and montmorillonite. Geochimica et Cosmochimica Acta 74, 1999–2010.

Glaus, M.A., Loon, L.R. van, Laer, L. van, Aertsens, M., Bruggeman, C., Govaerts, J., Maes, N., 2013. Benchmark experiments for the investigation of the diffusive behaviour of 85Sr2+ in compacted Na-illite, In: Migration, Loughborough.

Guimarães, L. D. N., Gens, A. Sánchez, M. Olivella S. A chemo-mechanical constitutive model accounting for cation exchange in expansive clays. Géotechnique 63, 221-234 (2013).

Holmboe, M. and Bourg, I.C., 2014, Molecular dynamics simulations of water and sodium diffusion in smectite interlayer nanopores as a function of pore size and temperature, J. Phys. Chem. C, 118, 1001-1013.

Holmboe, M., Wold, S., Jonsson, M., 2012. Porosity investigation of compacted bentonite using XRD profile modeling. Journal of Contam. Hydrol. 128, 19–32.

Klinkenberg, L.J. The Permeability of Porous Media to Liquids and Gases, in API Drilling and Production Practice, 200–213 (1941).

Kozaki T., Inada K., Sato S., Ohashi H., 2001, Diffusion mechanism of chloride ions in sodium montmorillonite. J. Contam. Hydrol., 47, 159-170.

Lenhard, R., Fedors, R., Manepally, C., Pabalan, R., Ofoegbu, G., Chiang, K., Bradbury, J., Markley, C. Buffer and backfill workshop report, U.S. Nuclear Regulatory Commission, Contract NRC–02–07–006, 2011.

Likos, W. J. and Wayllace, A. Porosity evolution of free and confined bentonites during interlayer hydration. Clays and Clay Minerals 58(3): 399-414 (2010).

Mitchell J., Soga, K. Fundamentals of Soil Behavior, Third edition, John Wiley & Sons, INC. ISBN-13: 978-0471463023, (2005).

Molera, M. and Eriksen, T., 2002, Diffusion of $^{22}Na^{+}$, $^{85}Sr^{2+}$, $^{134}Cs^{+}$ and $^{57}Co^{2+}$ in bentonite clay compacted to different densities: experiments and modeling, Radiochim. Acta 90, 753–760.

Molera, M., Eriksen, T., Jansson, M., 2003, Anion diffusion pathways in bentonite clay compacted to different dry densities, Applied Clay Science 23, 69–76.

Nutt, M., Used Fuel Disposition Campaign Disposal Research and Development Roadmap (FCR&D-USED-2011-000065 REV0), U.S. DOE Used Fuel Disposition Campaign, 2011.

OECD, Engineering barrier systems and the safety of deep geological repositories (State-of-the-art Report), ISBN 92-64-18498-8, 2003.

Olivella, S., Gens, A. Vapour transport in low permeability unsaturated soils with capillary effects. Transport In Porous Media, 40, 219–241 (2000).

Parkhurst, D.L. and Appelo, C.A.J., 1999. User's guide to PHREEQC (version 2) - a computer program for speciation, reaction-path, 1D-transport, and inverse geochemical calculations. US Geol. Surv. Water Resour. Inv. Rep. 99-4259, 312p.

Pousada, P.E. Deformabilidad de arcillas expansivas bajo succión controlada. Ph. D. Thesis, Technical University of Madrid, Spain (1982).

Pusch, R., Knutsson, S., Mohammed, M.H. Isolation of hazardous waste in crystalline rock, Journal of Earth Sciences and Geotechnical Engineering, vol.2, no. 3, 57-75, 2012.

Rutqvist J., Barr D., Birkholzer J.T., Chijimatsu M., Kolditz O., Liu Q.-S., Oda Y, Wang W.-Q. and Zhang C.-Y. Results from an international simulation study on coupled thermal, hydrological, and mechanical (THM) processes near geological nuclear waste repositories. Nuclear Technology, 163, 101–109 (2008).

Rutqvist, J., Ijiri, Y. Yamamoto, H. Implementation of the Barcelona Basic Model into TOUGH-FLAC for simulations of the geomechanical behavior of unsaturated soils. Computers & Geosciences, 37, 751–762 (2011).

Rutqvist, J., Zheng, L., Chen, F., Liu, H.-H., Birkholzer, J. Modeling of coupled thermo-hydro-mechanical processes with links to geochemistry associated with bentonite-backfilled repository tunnels in clay formations. Rock Mech. Rock Eng., 47, 167–186 (2014).

Sánchez, M., Gens, A., Guimarães, L. do N., Olivella, S. A double structure generalized plasticity model for expansive materials. Int. J. Numer. Anal. Meth. Geomech., 29, 751–787 (2005).

Sánchez, M., Gens, A., Olivella, S. THM analysis of a large-scale heating test incorporating material fabric changes. Int. J. Numer. Anal. Meth. Geomech., 36, 391–421 (2012).

Sridharan, A., Rao, S. M. and Murthy, N. S. Compressibility behaviour of homoionized bentonites. Géotechnique 36, 551-564 (1986).

Tournassat, C., Appelo, C.A.J., 2011, Modelling approaches for anion-exclusion in compacted Na-bentonite. Geochimica et Cosmochimica Acta 75, 3698–3710.

Tournassat, C., Neaman, A., Villiéras, F., Bosbach, D., Charlet, L., 2003, Nanomorphology of montmorillonite particles: Estimation of the clay edge sorption site density by low-pressure gas adsorption and AFM observations. American Mineralogist 88, 1989–1995.

Xu, T., N. Spycher, E. Sonnenthal, G. Zhang, L. Zheng and K. Pruess. TOUGHREACT Version 2.0: A simulator for subsurface reactive transport under non-isothermal multiphase flow conditions. Computers & Geosciences 37(6): 763-774 (2011).